

AD-A080 934

ARIZONA UNIV TUCSON OPTICAL SCIENCES CENTER  
OPTIMUM OPTICAL STRUCTURES FOR ACTIVE CONTROL.(U)  
JAN 80 R R SHANNON, R M RICHARD, J G HANSEN

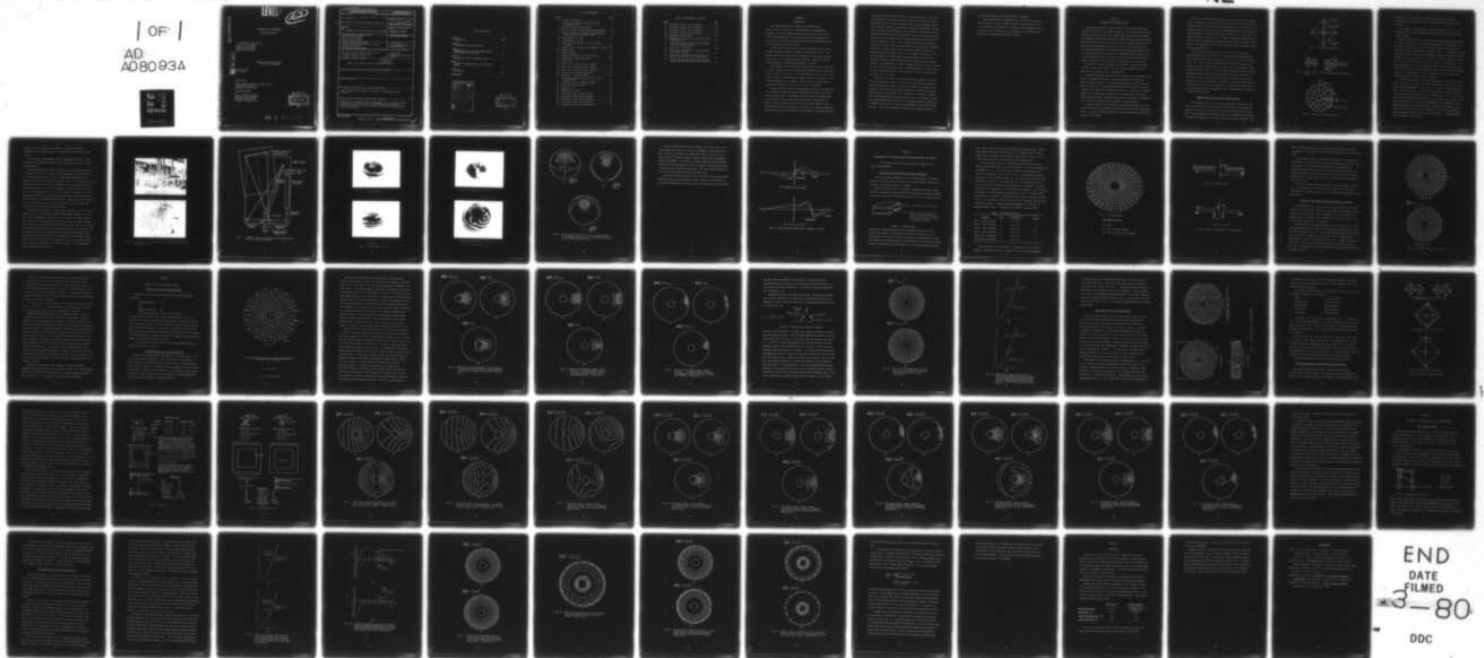
F/G 20/6

N00014-78-C-0282

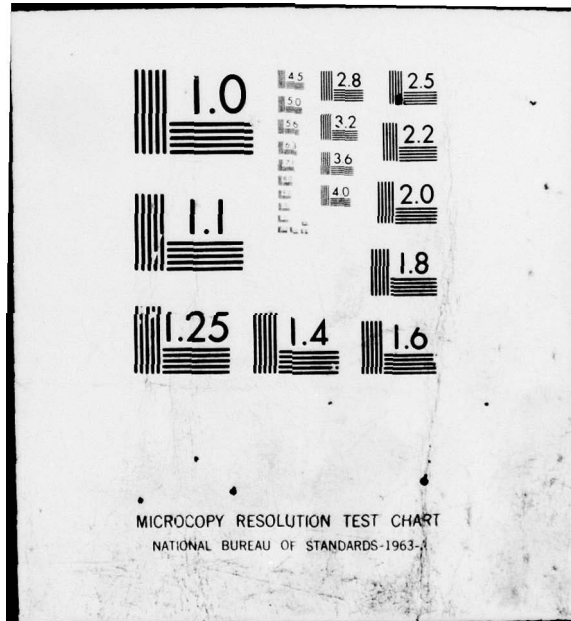
UNCLASSIFIED

NL

| OF |  
AD  
A080934



END  
DATE  
FILMED  
3-80  
DDC



**LEVEL #**

**12**

55

ADA 080934

**OPTIMUM OPTICAL STRUCTURES  
FOR ACTIVE CONTROL**

R. R. Shannon, R. M. Richard  
and J. G. R. Hansen  
Optical Sciences Center  
University of Arizona  
Tucson, Arizona 85721

**DDC FILE COPY**

Approved for Public Release;  
Distribution Unlimited

21 January 1980  
Final Report

Prepared for

Defense Advanced Research Projects Agency  
1400 Wilson Boulevard  
Arlington, Virginia 22209

Monitoring Agency

Director, Physics Program  
Office of Naval Research  
800 North Quincy Street  
Arlington, Virginia 22217

**DDC  
RECEIVED  
FEB 14 1980  
REGULATED  
D**

80 2 14 016

Unclassified

SECURITY CLASSIFICATION OF THIS PAGE (When Data Entered)

REPORT DOCUMENTATION PAGE		READ INSTRUCTIONS BEFORE COMPLETING FORM
1. REPORT NUMBER	2. GOVT ACCESSION NO.	3. RECIPIENT'S CATALOG NUMBER
4. TITLE (and Subtitle)		5. TYPE OF REPORT & PERIOD COVERED
⑥ Optimum Optical Structures For Active Control		⑨ Final <i>Final report</i>
7. AUTHOR(s)		6. PERFORMING ORG. REPORT NUMBER
⑩ R. R. Shannon, R. M. Richard and J. G. R. Hansen		8. CONTRACT OR GRANT NUMBER(s)
9. PERFORMING ORGANIZATION NAME AND ADDRESS		10. PROGRAM ELEMENT, PROJECT, TASK AREA & WORK UNIT NUMBERS
Optical Sciences Center University of Arizona Tucson, Arizona 85721		
11. CONTROLLING OFFICE NAME AND ADDRESS		12. REPORT DATE
Defense Advanced Research Projects Agency 1400 Wilson Boulevard Arlington, Virginia 22209		15 December 1979
14. MONITORING AGENCY NAME & ADDRESS (if different from Controlling Office)		13. NUMBER OF PAGES
Director, Physics Program, Office of Naval Research, 800 North Quincy Street, Arlington, Virginia 22217		61
15. SECURITY CLASS. (of this report)		15a. DECLASSIFICATION/DOWNGRADING SCHEDULE
Unclassified		
16. DISTRIBUTION STATEMENT (of this Report)		
Approved for public release; distribution unlimited		
17. DISTRIBUTION STATEMENT (of the abstract entered in Block 20, if different from Report)		
⑪ 21 Jan 84		
18. SUPPLEMENTARY NOTES		
19. KEY WORDS (Continue on reverse side if necessary and identify by block number)		
Optics, Mirrors, Active Optics, Large Optics, Astronomical Optics Structures		
20. ABSTRACT (Continue on reverse side if necessary and identify by block number)		
A NASTRAN structural analysis of a lightweight mirror structure has been completed and is compared with previous experimental measurements. A preliminary design for a 4-meter aperture, 6-meter focal length primary mirror is presented.		

DD FORM 1 JAN 73 1473

402821

Unclassified  
SECURITY CLASSIFICATION OF THIS PAGE (When Data Entered)

SP

TABLE OF CONTENTS

Chapter 1	Page
INTRODUCTION . . . . .	1
Chapter 2	
INTEGRATED ACTIVE MIRROR SYSTEMS . . . . .	4
Chapter 3	
PRELIMINARY SAP IV AND MSC/NASTRAN FINITE ELEMENT MODELS AND ANALYSIS . . . . .	15
Chapter 4	
ANALYSIS TO DESIGN 40-ACTUATOR SYSTEM . . . . .	22
Chapter 5	
ANALYSIS TO EVALUATE DESIGN OF 40-ACTUATOR SYSTEM . . . . .	48
Chapter 6	
CONCLUSIONS . . . . .	59
BIBLIOGRAPHY . . . . .	61

Accession For	
NTIS GRA&I	<input checked="" type="checkbox"/>
DDC TAB	<input type="checkbox"/>
Unannounced	<input type="checkbox"/>
Justification	<input type="checkbox"/>
By _____	
Distribution/	
Availability Codes	
Dist.	Avail and/or special
A	

DDC  
**RECEIVED**  
 FEB 14 1980  
**RECEIVED**  
 D

## LIST OF ILLUSTRATIONS

Figure	Page
1. Actuator configuration . . . . .	6
2. Section view of truss configuration along meridional plane . . . . .	6
3. Top view of truss configuration . . . . .	6
4. Two views of the 4 active actuator post systems . .	8
5. Schematic layout of holographic interferometric test of 60-cm active mirror model . . . . .	9
6. Slope changes, 0.4 zone . . . . .	10
7. z displacement, 0.4 zone . . . . .	11
8. Cubic spline contour plot of 4.8 in. radius actuator . . . . .	12
9. Surface profile through axis of symmetry, 0.4 zone	14
10. Sandwich model . . . . .	15
11. Flat plate model . . . . .	17
12. Supports and loads for flat plate models . . . . .	18
13. Homogeneous, annular flat plate . . . . .	20
14. Mirror model . . . . .	23
15. Mirror for 40 actuator system. (80 cm) . . . . .	25
16. Mirror for 40-actuator system. (160-cm) . . . . .	26
17. Mirror for 40-actuator system. (200-cm) . . . . .	27
18. Cross section of deflection pattern . . . . .	28
19. Mirror for 40 actuator system . . . . .	29
20. Deflection of radial cross section of mirror during defocus . . . . .	30
21. 40-actuator system. Undeformed shape . . . . .	32
22. Truss model and deflections . . . . .	34
23. Property set 1 . . . . .	36
24. Property sets 6 and 7 . . . . .	37
25. 40-actuator system, 80-cm actuator . . . . .	38
26. 40-actuator system, 160-cm actuator . . . . .	39
27. 40-actuator system, 200-cm actuator . . . . .	40
28. 40-actuator system, 80-cm actuators . . . . .	41
29. 40-actuator system, 160-cm actuators . . . . .	42

LIST OF ILLUSTRATIONS--Continued

Figure		Page
30.	40-actuator system, 200-cm actuators . . . . .	43
31.	40-actuator system, 80-cm actuators . . . . .	44
32.	40-actuator system, 160-cm actuators . . . . .	45
33.	40-actuator system, 200-cm actuators . . . . .	46
34.	Approximate thermal model . . . . .	48
35.	Deflection of radial cross section of mirror during defocus . . . . .	51
36.	Deflection of radial cross section of mirror heated by thermal gradient . . . . .	52
37.	Contour plots for defocus . . . . .	53
38.	Contour plot of deflection of mirror heated by thermal gradient . . . . .	54
39.	Contour plots of deflection from actuator normal position and radial slope control . . .	55
40.	Contour plots of heated mirror after actuator normal position and radial slope control . . .	56

## CHAPTER I

### INTRODUCTION

This report discusses the completion of work done over several years on a concept for a large semi-active primary mirror structure. The major innovation reported on here is the concept of a totally integrated support structure and mirror that incorporates not only position control but also slope control in two principal directions at each actuator point on the surface.

Previous work on this subject has been discussed in a prior report (Shannon and Smith, 1978) plus a Master's thesis (Radau, 1977). This present report fully analyzes one conceptual mirror structure that could be used for a 3- or 4-m aperture space telescope. These same concepts could be applied to a ground-based telescope if desired.

The fundamental concept consists of using either a simple, thin glass face plate or an extremely thin, lightweight structured glass or ultra-low expansion material face plate. This latter approach may be desirable under conditions when the maximum possible weight reduction is required. As will be seen by reference to the tables in Chapter 4, the weight estimate for this mirror is extremely low, being on the order of  $20 \text{ kg/m}^2$ .

The basic concepts involved in supporting the mirror face plate are the use of a number of similar triangular components that support and stiffen vertical support posts. These supports are attached to a substrate plate (not necessarily a stiff plate) that distributes the loads around the mirror. Several different concepts have been discussed over the years regarding the nature of the actuators to be used. The current recommended approach consists of providing axial force actuation. An actuator lengthens

and shortens the central post of each of the actuator points. This force reacts through the triangular supports at each of the support locations. Originally the use of cables rather than rods for the triangular supports was considered. However, the advantage of being able to operate actuators both with compression and tension on the supports is sufficiently attractive that the original concept was modified. Surface slope corrections are obtained from an orthogonal pair of actuators that press on the center of the post causing it to warp. These tangential forces react through the back plate structure, which is reasonably stiff in the radial or tangential direction. As will be seen from the structural analysis as well as in previous experiments, proper choice of the stiffness of the mirror plate and the backing plate allows almost total decoupling of the influence functions in the tilt directions and the axial direction at each actuator location. This implies that an almost diagonal matrix will need to be solved in order to relate the control forces to the measured mirror surface errors. This will greatly simplify the control problem. In fact, open loop operation appears to be feasible.

Connection of the mirror to the spacecraft or ground-based telescope will be accomplished by kinematic connection of three points located near principal actuator locations. For spacecraft usage these torque loads will generally be small and will be caused primarily by mechanical vibrations, thermal changes, or acceleration due to slewing of the vehicle. Therefore, no particular attention has been paid to this part of the mounting problem. For a ground-based system, there will be considerably greater problems due to constant acceleration of gravity, which changes as the telescope tracks an object. Some active components working with the kinematic supports to

counter the telescope loads would probably be advisable.

The work reported here constitutes one of the principal technical efforts carried out under the DARPA contract. This work constitutes a novel application of mechanics to the mirror mounting problem. Sufficient details are presented here for interested users to determine the application of this approach to their problems.

## CHAPTER 2

### INTEGRATED ACTIVE MIRROR SYSTEMS

Integrated active mirror systems studied in this effort differ from other mirror systems in two important respects. First, each mirror actuator controls the surface in three ways--normal position and slope about radial and tangential axes--thereby reducing the number of points at which actuation must be applied to the mirror. Second, the mirror element forms part of the structure instead of being referenced to a much stiffer reference plate. The integrated active mirror and support have an increased efficiency since the loads are carried in the direction of maximum structural stiffness, i.e. in tensile-membrane action. The weight of the system is minimized when the membrane of the shell (the active mirror) becomes part of the structure.

The number of actuators required for a system is a function of several variables: the mirror stiffness, the scale of the residual errors, the magnitude of the residual errors, and their form.

Previous studies have indicated that scalloping of the outer edge of the mirror is a significant problem. Scalloping occurs when an attempt is made to defocus the mirror. In choosing the 40-actuator system for further study, the effects of scalloping have been alleviated by closer placement of actuators at the edge. This configuration allows for correction of residual errors with a minimum spatial frequency of  $D/5$ , when using only actuator normal position control. With both normal position and radial and tangential slope controls the minimum spatial frequency is reduced to  $D/10$ .

In order to increase the stiffness of the support structure, the truss and reference plate are integrated, as illustrated by the truss configuration in Fig. 1. Here the truss is modified to include the additional horizontal reference plate element.

Figure 2, a meridional section view of the structure of the 40-actuator system, illustrates the change in actuator truss height with radial position and the symmetry of the truss about the reference plate. The stiffness of the reference structure is increased by the spoke configuration created by this radial alignment. The width of the radial trusses is  $D/5$ . A top view of the support structure is shown in Fig. 3. Sixteen tangentially aligned trusses have been added at points where scalloping would have been maximized in their absence. The positions of these actuators make the width of the edge actuator trusses approximately  $D/5$ .

This 40-actuator system is identical to that of the 4-m-diameter mirror system analyzed in this report. Analyses used the MSC/NASTRAN and SAP IV finite element computer programs and includes the following mechanical loads: (1) loads to cause a displacement of one actuator control while keeping all other controls fixed, (2) loads to defocus the mirror in order to study scalloping, and (3) a thermal gradient through the mirror thickness. Experimental verification of the integrated active mirror concept and the associated structural analysis was made using a 41-actuator system with a 60-cm aperture  $f/1.5$  active mirror. The mirror in the 41-actuator-system has no central hole, and the truss configuration is modified by the addition of a central actuator with a 3-dimensional truss. The experimental verification is briefly discussed below.

#### Experimental Verification of 41-Actuator System

A 60-cm-aperture,  $f/1.5$  active mirror was designed to demonstrate the figure control efficiency of a 41-actuator support concept. This system was designed to show the localization of both the position and slope controls. Three of the actuators were implemented with active components, the remaining 38 were preset mechanically in each of their three degrees of freedom. For

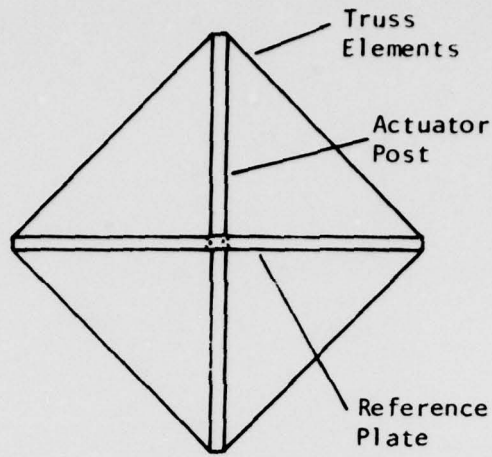


Fig. 1. Actuator configuration

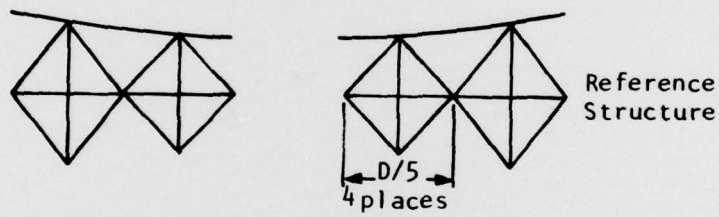


Fig. 2. Section view of truss configuration along meridional plane.

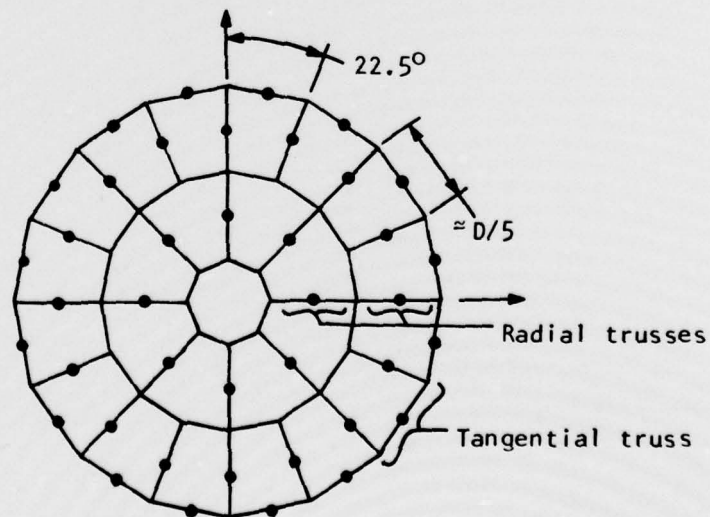


Fig. 3. Top view of truss configuration.

these three active actuators, each degree of freedom is controlled independently by a single servomotor. Photographs of the model are shown in Fig. 4.

The experimental arrangement is shown schematically in Fig. 5. Interferograms were produced and compared with contour plots from SAP IV finite element analyses.

Figure 6a shows the effect of a tangential slope change produced at the 0.4 zone (9.5-cm radius). It bears a good resemblance to the prediction of the computer model (see Fig. 8a). The fringe contour shapes appear very similar but are more localized than predicted. This is to be expected, because the computer model was set up for a lightweight reference plate that is more flexible than the plate used in the experiment. Several fringes due to overall curvature change can be seen. This was caused by a change of one or two degrees Fahrenheit in the room temperature between the time the hologram was exposed and the time the interferogram was made. Some tilt is also noticeable, as well as irregularities due to air turbulence and reactions between the deformed shell and the fixed, passive actuators.

The deformation produced by a radial slope change also at the 0.4 zone is shown in Fig. 6b. The result of a small z-displacement is shown in Fig. 7a, and a large z-displacement is shown in Fig. 7b. Again, the fringe shapes are more or less as predicted (compare Figs. 8b and 8c), but are more localized. The reactions of the passive actuators are clearly seen in Fig. 7b. It should be noted that the peak occurring at about three o'clock at the 0.4 zone is not an actuator reaction, but an artifact introduced by the experimenter while demonstrating the real-time nature of the holographic interferometry--finger pressure on the back of the shell, estimated at 5 to 10 lb, apparently produced a permanent deformation in the form of a dimple. It was subsequently removed by making a new hologram.

these three active actuators, each degree of freedom is controlled independently by a single servomotor. Photographs of the model are shown in Fig. 4.

The experimental arrangement is shown schematically in Fig. 5. Interferograms were produced and compared with contour plots from SAP IV finite element analyses.

Figure 6a shows the effect of a tangential slope change produced at the 0.4 zone (9.5-cm radius). It bears a good resemblance to the prediction of the computer model (see Fig. 8a). The fringe contour shapes appear very similar but are more localized than predicted. This is to be expected, because the computer model was set up for a lightweight reference plate that is more flexible than the plate used in the experiment. Several fringes due to overall curvature change can be seen. This was caused by a change of one or two degrees Fahrenheit in the room temperature between the time the hologram was exposed and the time the interferogram was made. Some tilt is also noticeable, as well as irregularities due to air turbulence and reactions between the deformed shell and the fixed, passive actuators.

The deformation produced by a radial slope change also at the 0.4 zone is shown in Fig. 6b. The result of a small z-displacement is shown in Fig. 7a, and a large z-displacement is shown in Fig. 7b. Again, the fringe shapes are more or less as predicted (compare Figs. 8b and 8c), but are more localized. The reactions of the passive actuators are clearly seen in Fig. 7b. It should be noted that the peak occurring at about three o'clock at the 0.4 zone is not an actuator reaction, but an artifact introduced by the experimenter while demonstrating the real-time nature of the holographic interferometry--finger pressure on the back of the shell, estimated at 5 to 10 lb, apparently produced a permanent deformation in the form of a dimple. It was subsequently removed by making a new hologram.

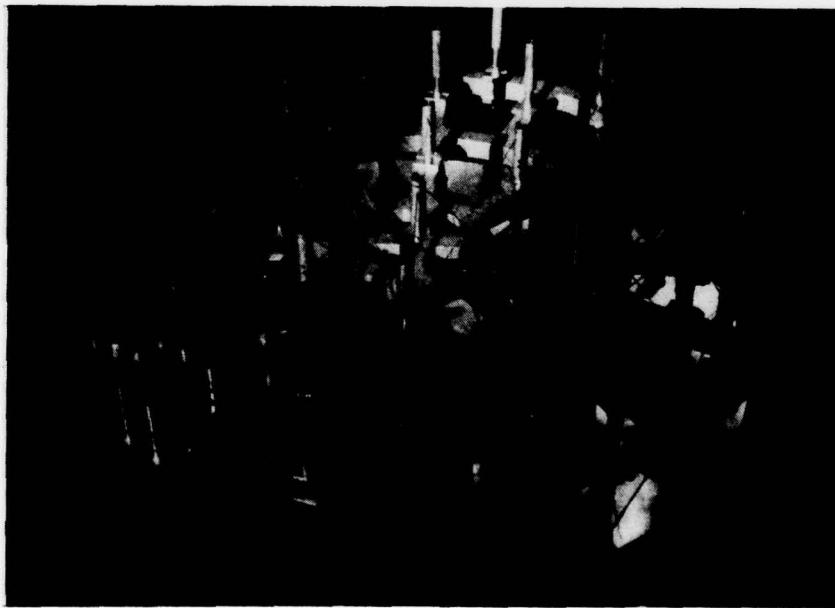
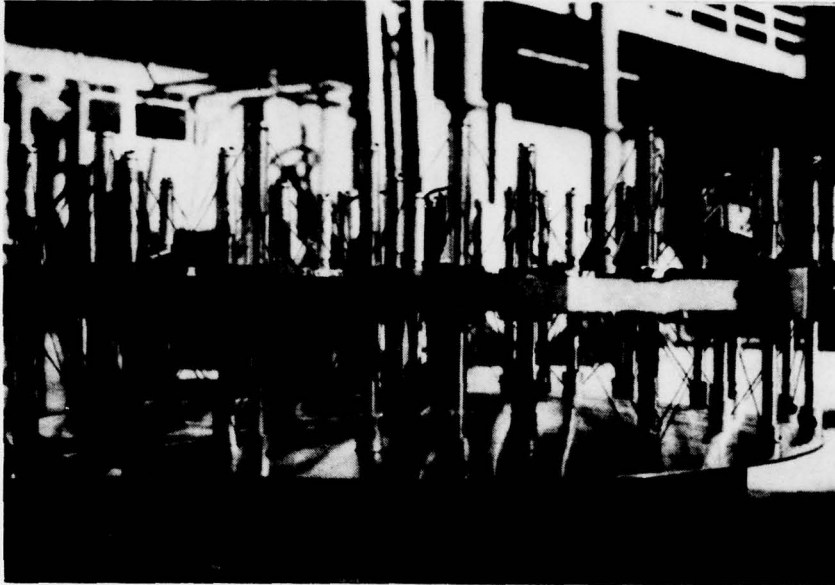


Fig. 4. Two views of the 4 active actuator post systems built for the experimental tests.

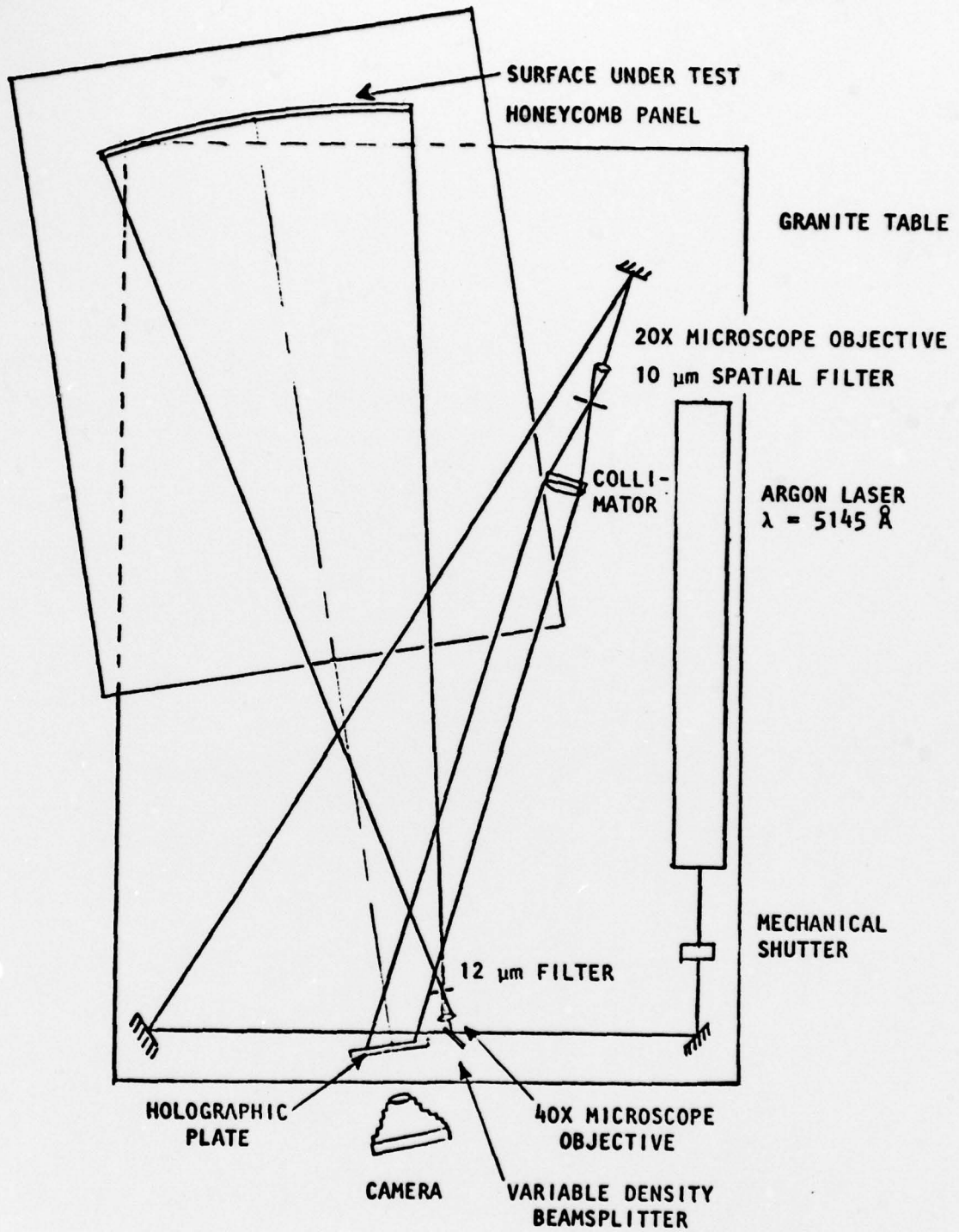
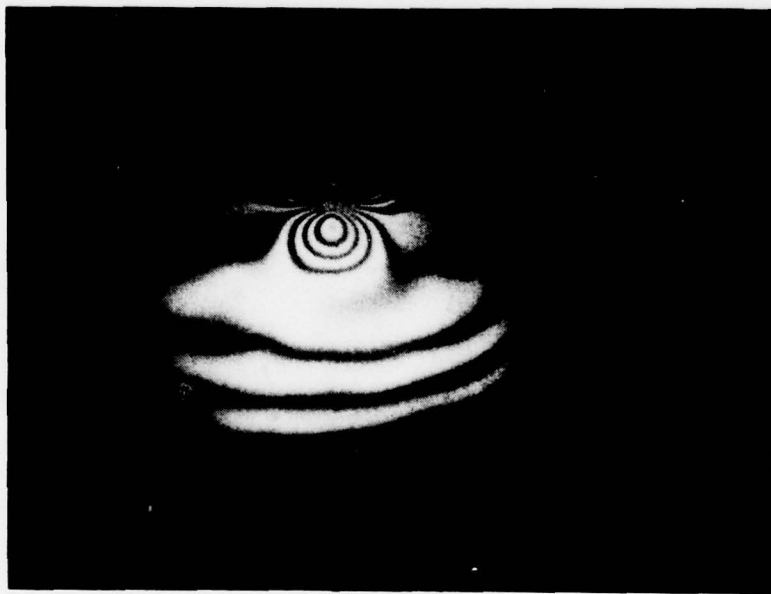


Fig. 5. Schematic layout of holographic interferometric test of 60-cm active mirror model.



(a) Tangential.

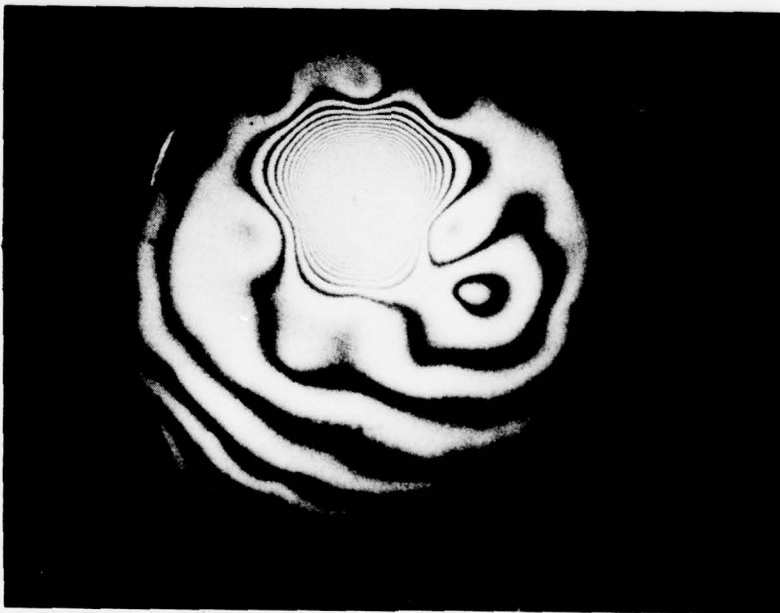


(b) Radial.

Fig. 6. Slope changes, 0.4 zone.

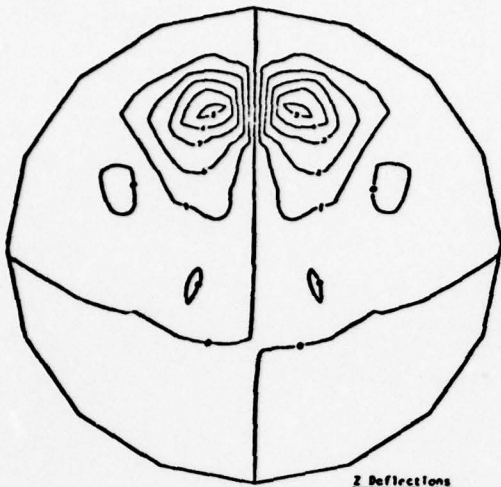


(a) Small displacement (no tilt).

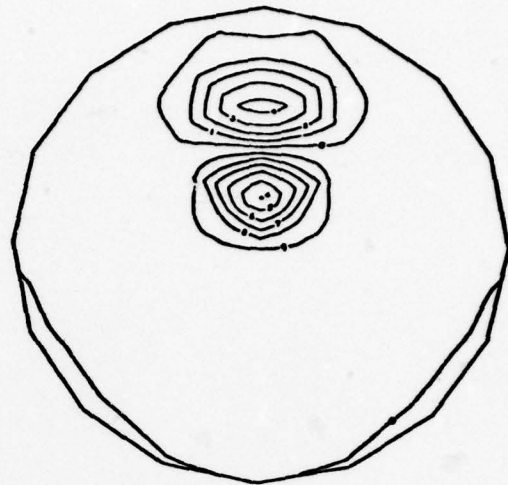


(b) Large displacement (28 fringes).

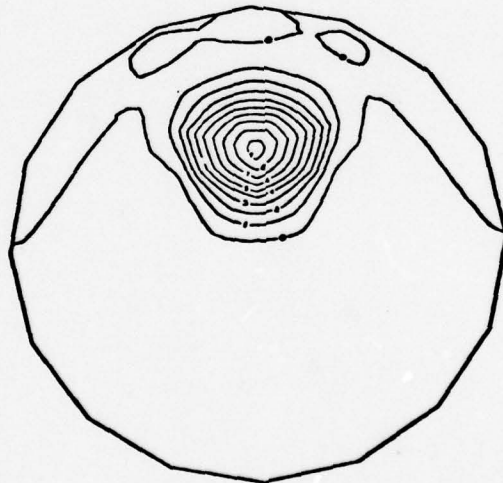
Fig. 7.  $z$  displacement, 0.4 zone.



(a) Z Deflections  
 Contour Interval =  $0.167 \times 10^{-4}$   
 Datum = 0.0



(b) Z Deflections  
 Contour Interval =  $0.566 \times 10^{-5}$   
 Datum = 0.0

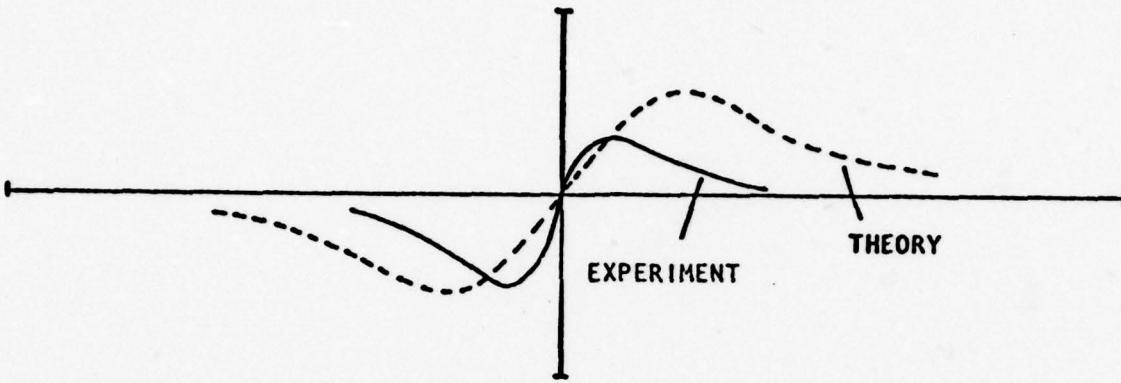


(c) Z Deflections  
 Contour Interval =  $0.566 \times 10^{-5}$   
 Datum = 0.0

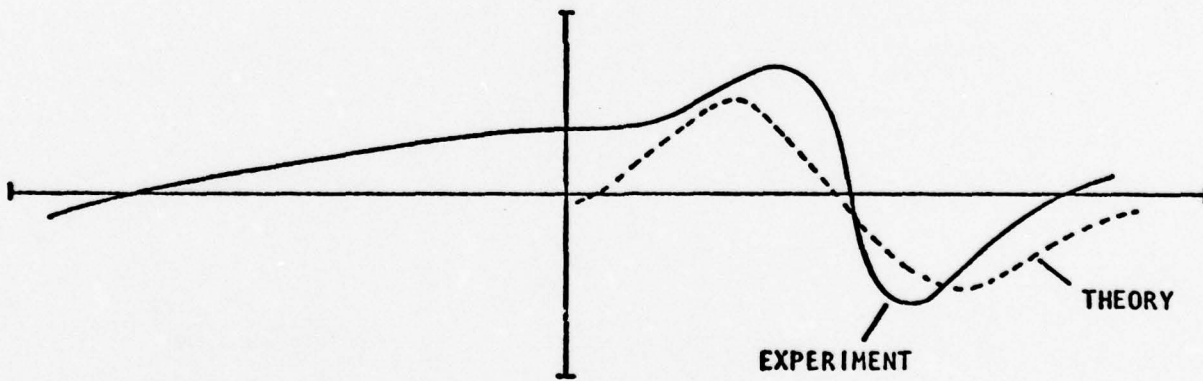
Fig. 8. Cubic spline contour plot of 4.8 in. radius actuator.  
 (a) Tangential slope control, (b) radial slope control,  
 and (c) normal position control.

Surface profiles along the axes of symmetry in the directions of the slope changes were computed by hand for the tangential slope change mode of Fig. 6a and for the radial slope change mode of Fig. 6b at the 0.4 zone. These profiles are plotted in Figs. 9a and 9b along with the corresponding computer predictions. The shapes are similar; however, the peak-to-valley separation in the experimental profiles is less than predicted--particularly in the case of the tangential slope change. Thus, the deformations appear to be more localized than predicted, as already noted.

A much more detailed accounting of the 40-actuator finite element model, mechanical design of the demonstration model, holographic interferometry of the model and comparison of results are included in Shannon and Smith (1978).



(a) Tangential slope change.



(b) Radial slope change

Fig. 9. Surface profile through axis of symmetry, 0.4 zone.

## CHAPTER 3

### PRELIMINARY SAP IV AND MSC/NASTRAN FINITE ELEMENT MODELS AND ANALYSIS

Two computer programs were used to model a sandwich plate--  
SAP IV and MSC/NASTRAN.

#### Preliminary SAP IV Finite Element Model and Analysis

The finite element modeling of structures representative of a sandwich mirror was initiated using the SAP IV finite element computer program on the University of Arizona CDC Cyber 175 computer.

The SAP IV program does not incorporate sandwich plate finite elements. Therefore, a segment of sandwich material was modeled using membrane elements as top and bottom faces and a solid element for the core, as shown in Fig. 10.

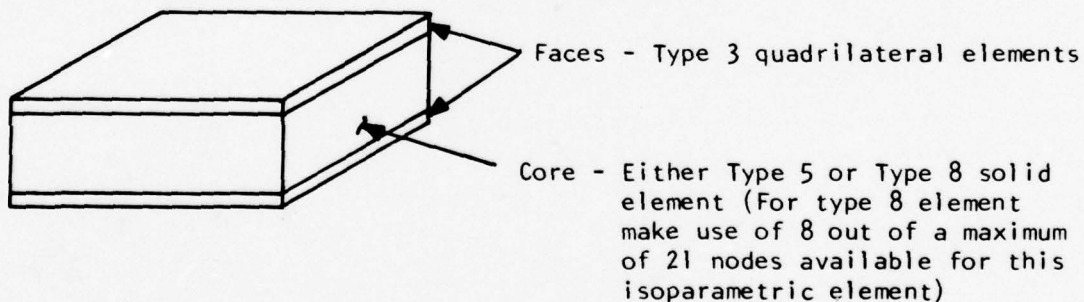


Figure 10. Sandwich model.

Incompatible displacement modes improve the bending properties of Type 3 quadrilateral elements for bending in the plane of the element, i.e. for bending moment vectors with directions perpendicular to the elements. Since the loading of the sandwich beam and mirror models will not cause this in-plane bending, incompatible displacement modes are not used for the quadrilaterals.

Type 5 solid elements also utilize incompatible displacement modes. Without these modes the element would be overly stiff in bending, since the basic element does not adequately represent the shear strain of bending. Type 8 solid elements do not utilize incompatible displacement modes.

Two finite element models of a homogeneous, annular flat plate were analyzed and compared with theoretical calculations. The finite element models are shown in Fig. 11. The only difference between the two models is the type of solid elements, either Type 5 or Type 8. The geometry and material properties of the two models are identical. In order to compare results with an analytical solution, (1) the plates are flat, not spherical, as in the actual mirror and (2) the plates are homogeneous, not honeycomb, so material properties for the membrane and solid elements are identical. In the analyses the models were simply supported along the outer edge. Two distinct loads were applied to each model. These loads and the support conditions are shown in Fig. 12. The following theoretical results were calculated using equations presented in Chapter 3 of Theory of Plates and Shells by Timoshenko and Woinowsky-Krieger (1959). A comparison of results is given in Table 1.

Table 1. Theoretical Results

<u>Analysis</u>	<u>Load</u>	<u>Max Deflection w(r=b)</u>	<u>% Error</u>
SAP IV - Type 5 elements	q	$1.21 \times 10^{-1}$	4
SAP IV - Type 5 elements	$Q_0$	$1.26 \times 10^{-6}$	3
SAP IV - Type 8 elements	q	$2.05 \times 10^{-2}$	84
SAP IV - Type 8 elements	$Q_0$	$2.26 \times 10^{-7}$	83
Plate Theory (Timoshenko)	q	$1.26 \times 10^{-1}$	--
Plate Theory (Timoshenko)	$Q_0$	$1.30 \times 10^{-6}$	--

The performance of Type 5 elements is far superior to that of Type 8 elements. Inaccuracies for Type 5 elements due to utilizing incompatible

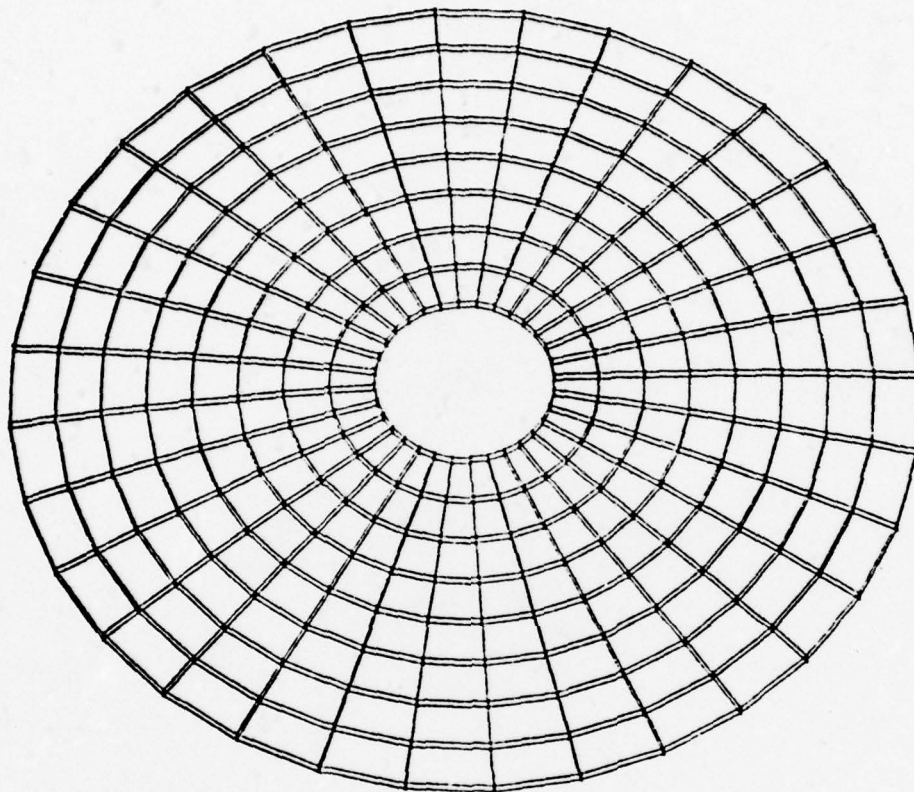


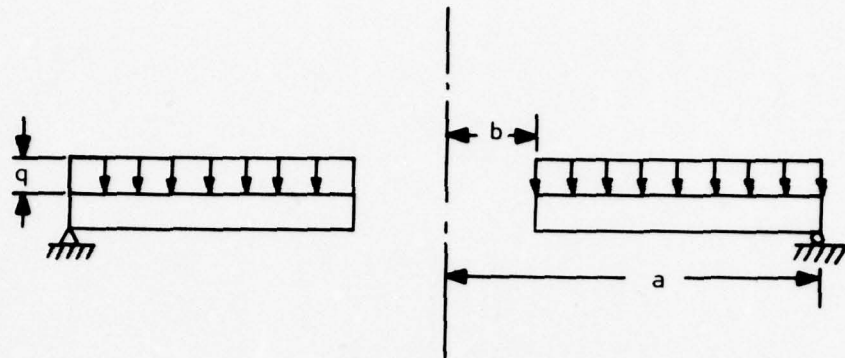
Fig. 11. Flat plate model.

Model Specifications:

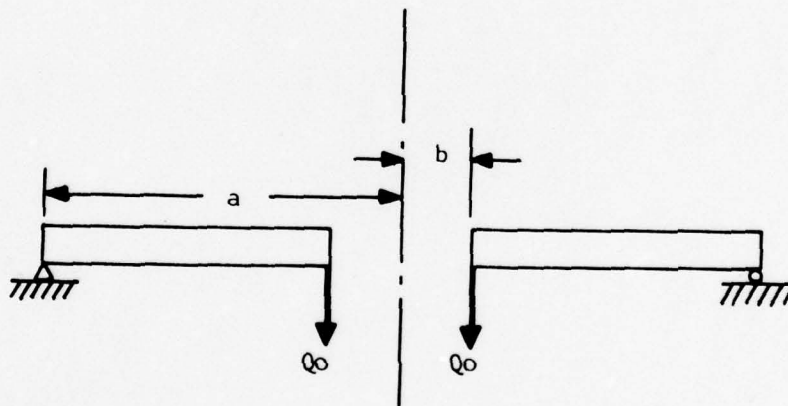
576 Nodes

512 Type 3 membrane elements

256 Type 5 or Type 8 solid elements



Uniform Distributed Load  $q$



Uniform Shear Load  $Q_0$

Fig. 12. Supports and loads for flat plate models.

modes for elements that are not rectangular parallelepipeds are trivial as compared to inaccuracies for Type 8 elements which do not use incompatible modes.

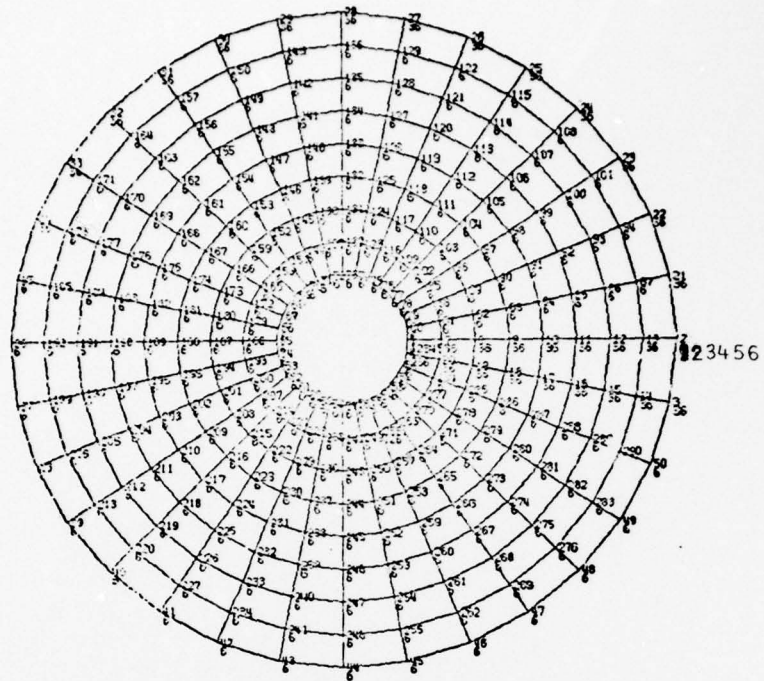
The honeycomb, spherical mirror model was generated by making minor modifications to the model of the homogeneous, annular flat plate with Type 5 solid elements. These modifications consisted of modifying the node coordinates perpendicular to the plate to achieve a spherical shape, and reducing the moduli of elasticity and rigidity of the core to 10% of that of solid material. Results from an analysis of the spherical mirror model are shown in Fig. 20.

The costs of running these SAP IV analyses were approximately \$125 per run. It became clear at this point that the analysis of the 40-actuator system would be prohibitive using SAP IV. By switching to NASTRAN, the costs were reduced.

#### Preliminary MSC/NASTRAN Finite Element Models and Analysis

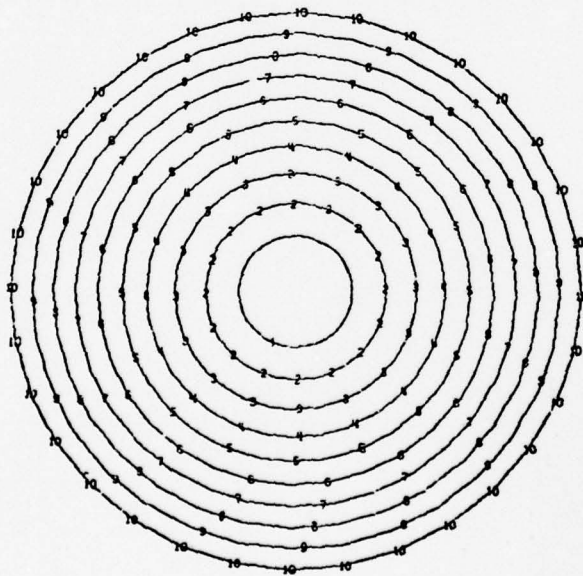
The MSC/NASTRAN finite element computer program is superior to the SAP program for our particular application, since NASTRAN has nonhomogeneous plate elements that can be used to model a sandwich plate. For a segment of a sandwich plate, one NASTRAN plate element models the two faces and the core, whereas three elements were needed with SAP.

A NASTRAN model of the same homogeneous, annular flat plate used in the previously described SAP IV analysis was generated with CQUAD4 plate elements. This model is shown in Fig. 13a. The model was analyzed under gravity loading and the results were compared to plate theory. For the NASTRAN model the deflection was  $1.24 \times 10^{-1}$ , giving an error of 1.6%. The SAP IV analysis has a 4% error. A contour plot of deflection normal to the plate is shown in Fig. 13b. The computer cost of this NASTRAN analysis was approximately 10% of the SAP IV analysis.



(a) NASTRAN model.

MAX-DEF. = 0.  
 MIN-DEF. =  $-1.24 \times 10^{-1}$



(b) Contour plot.

Fig. 13. Homogeneous, annular flat plate.

All of the contour plots in this report are for the z-displacement of the surface of the mirror. Each plot has ten displacement contours. To calculate the value of displacement for a particular contour line, refer to the maximum and minimum values on each figure. The maximum value occurs at contour line 10 and the minimum at contour 1. The contour intervals are constant and are one-ninth of the total difference between the extreme values. Displacement units are centimeters.

The shape of the deflection surface is the critical information gleaned from the contour plots. For linear analysis, the displacement coordinates for the surface are proportional to the magnitude of the load.

MSC/NATRAN has another feature, cyclic symmetry analysis, that is not available with SAP IV and that may be applied in future work. In cyclic symmetry, or rotational symmetry, one segment of a model is supplied by the user and the program transforms the properties of that segment to assimilate a model in which the fundamental segment is repeated at equal intervals about an axis of symmetry. Applied loads in the analysis can be applied over the entire model and do not have to be symmetrically located with respect to the axis of symmetry. Advantages to using this technique include only having to model one segment of a cyclic symmetric structure and reduction in computer costs in most situations. A disadvantage is that NASTRAN provides only a contour plot of the fundamental segment. In addition, both the structure and its boundary conditions must be symmetric in order to use cyclic symmetry, so at best, a structure mounted on a three-point support can be reduced to one third of the model.

Testing to date has shown cyclic symmetry to not be economically feasible when total program costs are considered. However, the cyclic symmetry capability in NASTRAN is being upgraded, and as models become more complex it may be desirable, if not essential, to make use of this capability.

## CHAPTER 4

### ANALYSIS TO DESIGN 40-ACTUATOR SYSTEM

#### 40-Actuator Mirror Finite Element Model

The mirror for the 40-actuator system has the following physical dimensions:

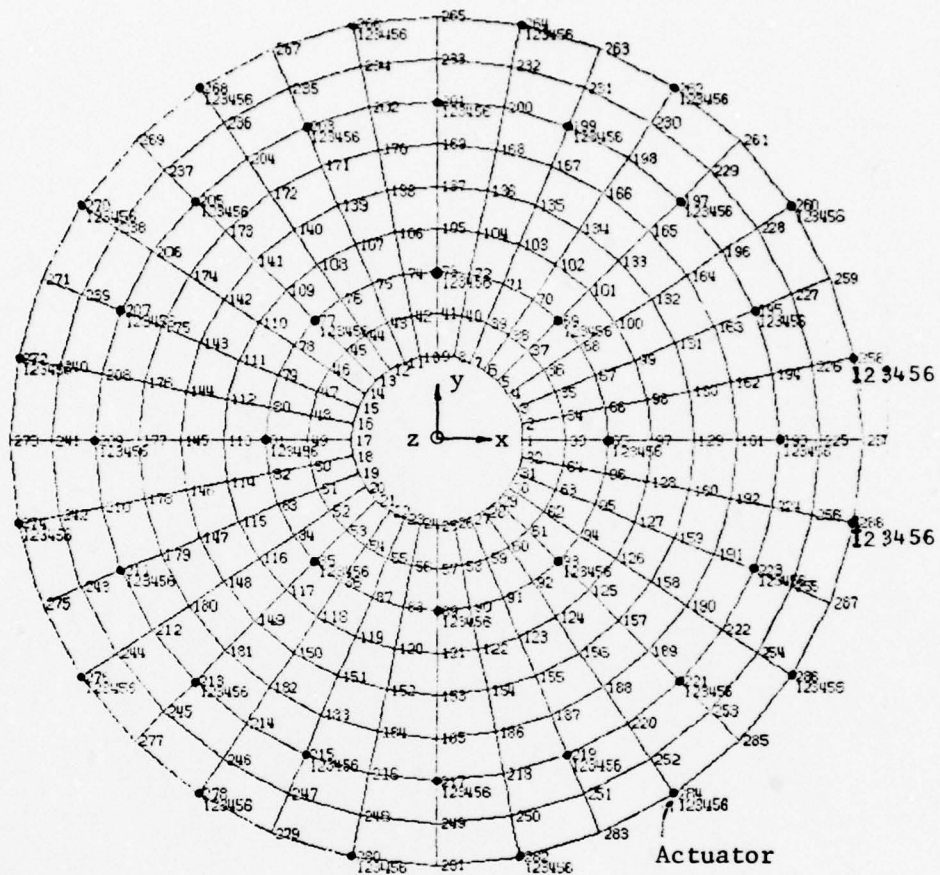
Diameter (Aperture)	4 m
f/no.	1.5
Radius of Curvature	12 m
Central Hole Diameter	80 cm or 20% of aperture

This model differs from the flat, annular plate model only in the z coordinates of the nodes. The mirror model is shown as a top view in Fig. 14a and as a side view in Fig. 14b. The locations on the mirror where actuators would attach are designated on the top view. The numbers on that plot are grid point numbers, and directly beneath selected grid numbers are the numbers of constrained degrees of freedom. The model is composed of 256 quadrilateral sandwich plate elements and 288 grid points.

A cross section of the mirror used in the following NASTRAN analyses is shown in property set 1, Fig. 23.

#### MSC/NASTRAN Analysis of 40-Actuator Mirror

Analyses of the mirror model were performed to aid in the design of the mirror and its support structures. The primary concern in this aspect of mirror design is to minimize scalloping around the outer and inner edges of the mirror due to defocus. Even though the support structure is not included in this model, a "perfectly rigid" support can be represented by constraining the motion of actuator degrees of freedom. Results of these analyses then serve as a guide in designing the support structure.



(a) Top view.



(b) Side View.

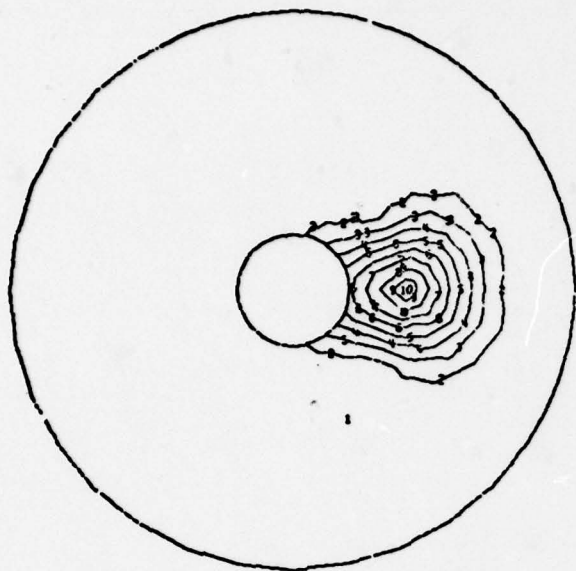
Fig. 14. Mirror model.

Actuators are located on three different radii in the 40-actuator system. Each actuator has normal position control and tangential and radial slope control. This makes nine unique controls which must be analyzed. For each control, all actuator degrees of freedom are fixed except for the degree of freedom being given a unit displacement. Contour plots of the mirror's z displacement, shown in Figs. 15 through 17, represent each of the nine unique controls. Note how the deformations are localized to the immediate vicinity of the displaced actuator. If one were to mark the actuator locations on these contour plots, one would see that in every case all contour lines drawn are contained within the region bounded by the actuators neighboring the displaced actuator. These localized deflections reduce coupling between actuator controls and significantly reduce the complexity of the required control system. These contour plots will be compared to those from an analysis of 40-actuator systems where support systems have finite stiffness.

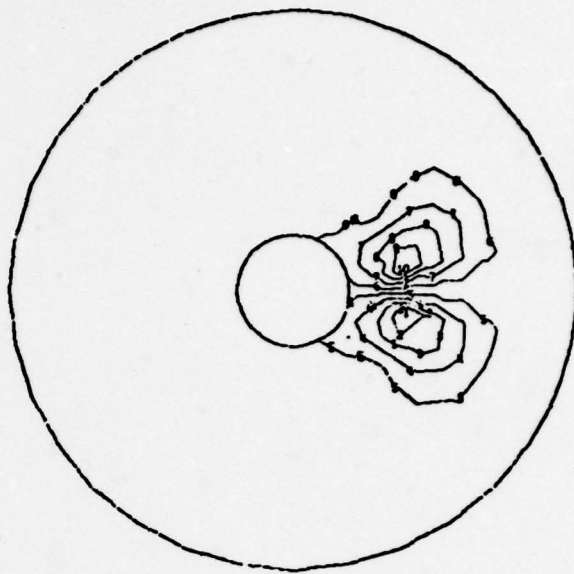
Scalloping, which was demonstrated early in our active optics studies, is a result of attempts to make slight changes in the radius of curvature. A pure radius change of the shell of the mirror would require a state of stress that had, for its boundary conditions, a uniform radial membrane stress due to a uniform pressure applied to the surface of the shell. Bending and shear stresses along the boundary would not exist. In attempting to produce this change through the bending of the shell by a discrete number of actuator points, deflections that are functions of angular position are obtained. Since the membrane stiffness (the stiffness associated with middle surface stretching) for the mirror is several orders of magnitude larger than the bending stiffness (the stiffness associated with the formation of a "develorable" shape), and these are coupled in shell action, the membrane stiffness effect dominates, forcing considerable bending to occur in order to accommodate the enforced displacements at the actuator points. Since for a homogeneous plate the membrane stiffness varies with  $t$ , the thickness of

MAX-DEF. = 1.00  
MIN-DEF. = - 2.98 x 10<sup>-2</sup>

MAX-DEF. = 5.01  
MIN-DEF. = - 5.01

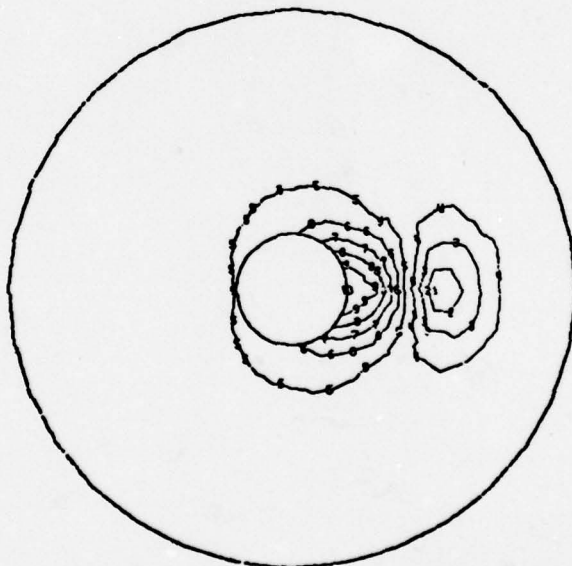


(a)



(b)

MAX-DEF. = 7.62  
MIN-DEF. = - 5.69

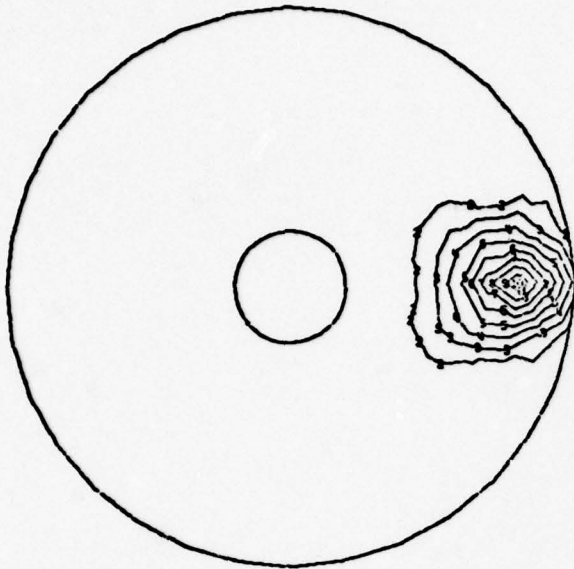


(c)

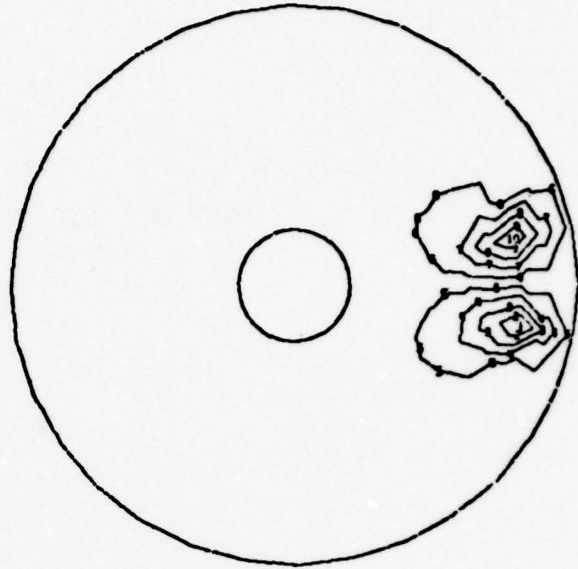
Fig. 15. Mirror for 40 actuator system. 80-cm actuators. (a) Normal position control, (b) tangential slope control, and (c) radial slope control. Property set 1.

MAX-DEF. = 1.00  
MIN-DEF. = - 4.07 x 10<sup>-2</sup>

MAX-DEF. = 4.43  
MIN-DEF. = - 4.43

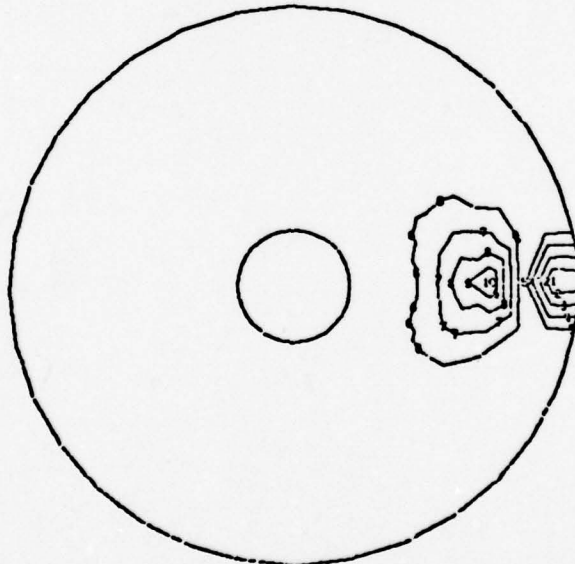


(a)



(b)

MAX-DEF. = 6.97  
MIN-DEF. = - 6.95

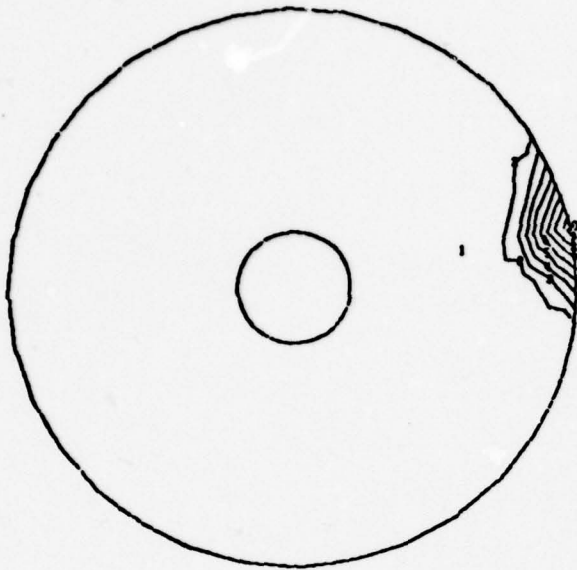


(c)

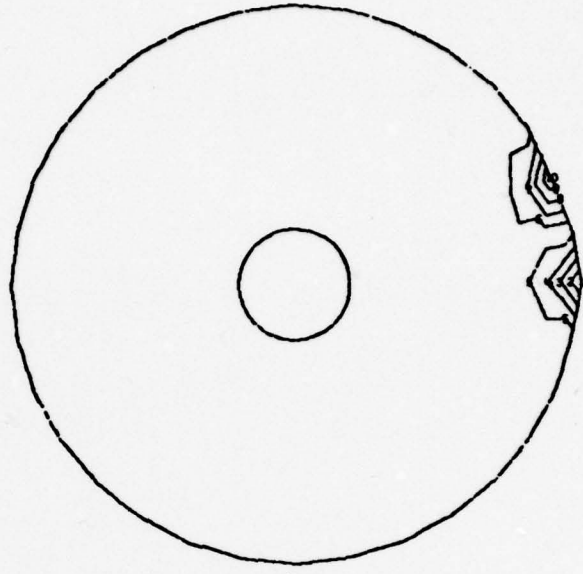
Fig. 16. Mirror for 40-actuator system. 160-cm actuators. (a) Normal position control, (b) tangential slope control, and (c) radial slope control. Property set 1.

MAX-DEF. = 1.00  
MIN-DEF. = - 3.43 x 10<sup>-2</sup>

MAX-DEF. = 6.62  
MIN-DEF. = - 6.62

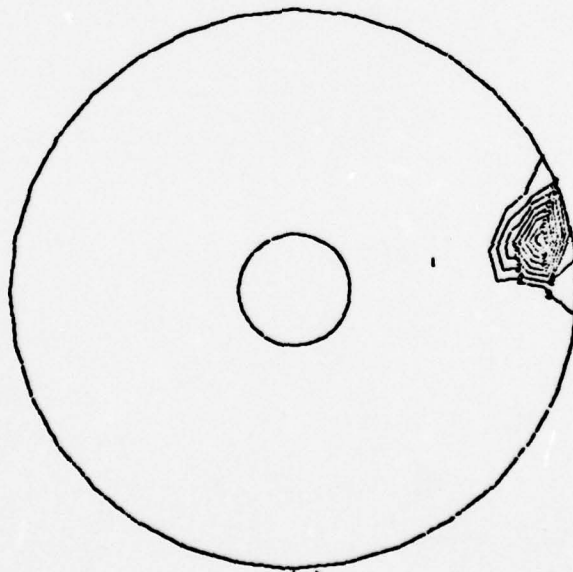


(a)



(b)

MAX-DEF. = 6.15  
MIN-DEF. = - 1.18 x 10<sup>-1</sup>



(c)

Fig. 17. Mirror for 40-actuator system. 200-cm actuators. (a) Normal position control, (b) tangential slope control, and (c) radial slope control. Property set 1.

the shell, and the bending stiffness with  $t^3$ , it is apparent that by increasing the mirror thickness, the scalloping effect may be reduced. An alternative to a thicker solid mirror is a mirror with sandwich construction and a lightweight core.

Scalloping ensues when the mirror is defocused. The deflection surface is an elliptic paraboloid. The equation for the paraboloid used for the  $z$  deflection,  $w$ , and a cross-sectional view of the resulting deflection pattern are shown in Fig. 18.

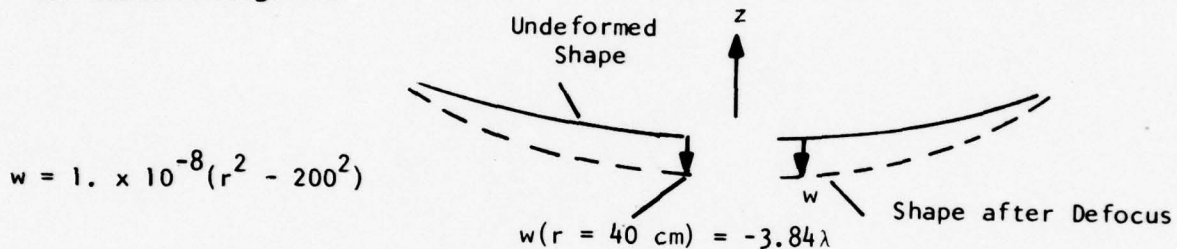
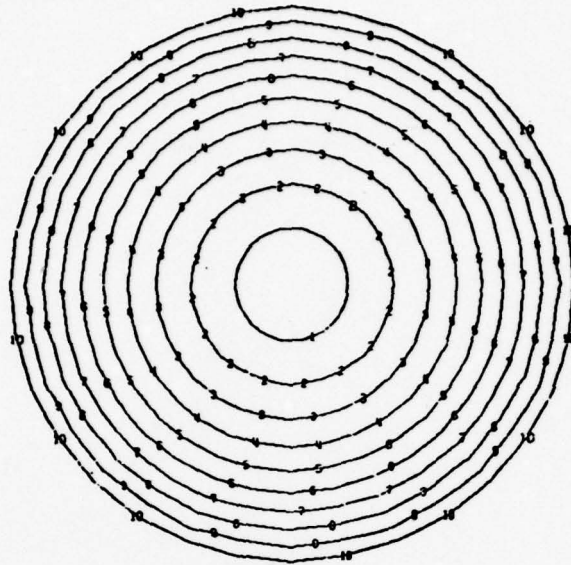


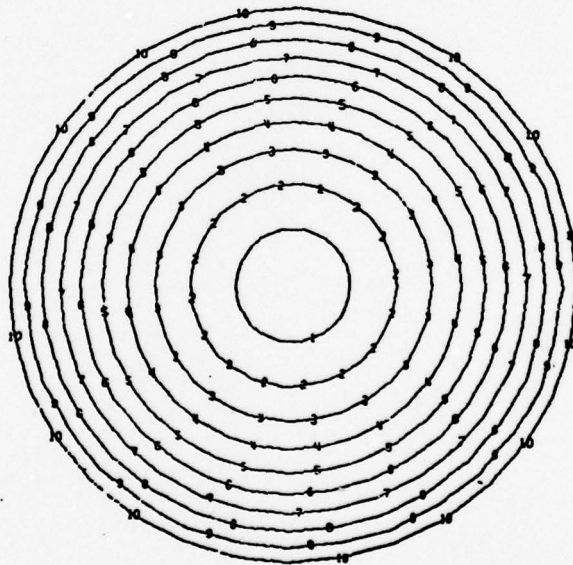
Figure 18. Cross section of deflection pattern.

Of course, since the analysis is linear, any convenient magnitude of displacement could have been chosen. This particular magnitude was chosen so that the deflection would be in units of  $\lambda$ , where both here and throughout this report  $\lambda = 1. \times 10^{-6}$  m. Vertical displacements and slopes were computed for each actuator location. Two separate analyses were executed. For the first, only deflections were enforced at the actuators. For the second, both deflections and slopes were enforced. Results are shown with contour plots, Figs. 19a and 19b, and in deflections of radial cross sections of the mirror, Figs. 20a and 20b. Note that the results for a similar SAP analysis are also included on the latter plots. For the SAP analysis, the mirror was modeled with separate elements for the two face sheets and the core, as described for the SAP flat plate model. Note the close correlation between SAP and NASTRAN results. The contour plots should be perfect circles and not flattened. To get a measure

MAX-DEF. = 0.  $10^{-4}$   
MIN-DEF. =  $-3.90 \times 10^{-4}$



MAX-DEF. = 0.  $10^{-4}$  (a)  
MIN-DEF. =  $-3.90 \times 10^{-4}$



(b)

Fig. 19. Mirror for 40-actuator system. Focus shift under (a) deflection control and (b) deflection and slope control. Property set 1.

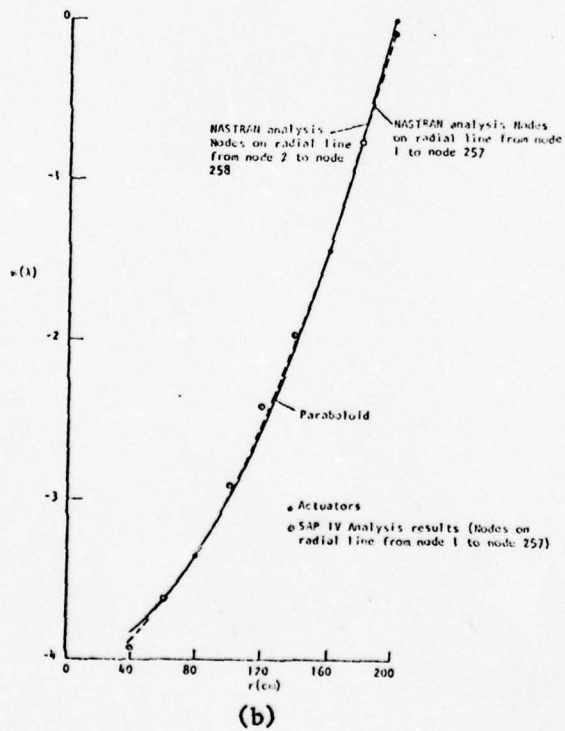
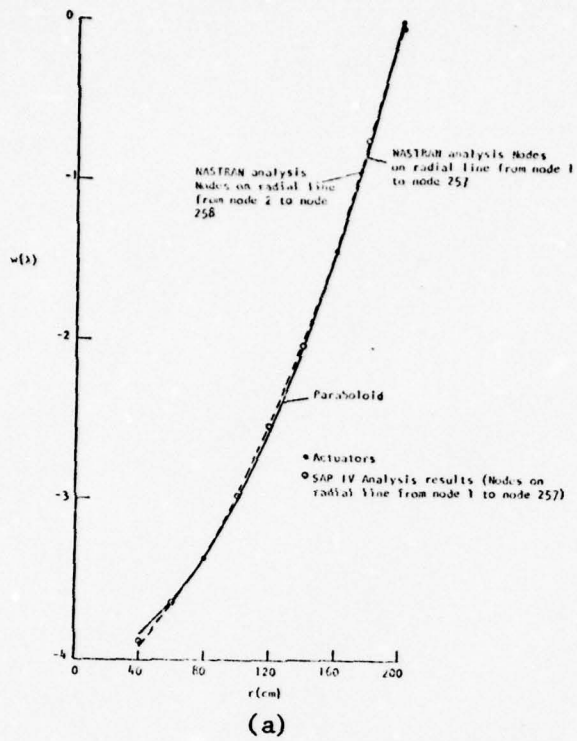


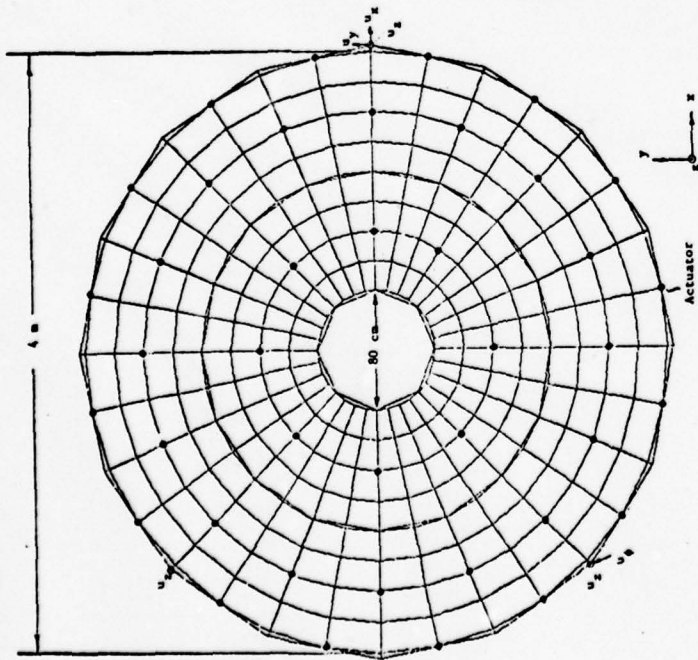
Fig. 20. Deflection of radial cross section of mirror during defocus with (a) only normal actuator normal position control, and (b) actuator normal position and radial slope controls. (Infinitely stiff support structure).

of the error due to the flattening of the contours, look at the plots of cross section deflection. These plots show that the error is largest at the inner and outer edges of the mirror. The severe scalloping exhibited in previous mirror designs has been all but eliminated. The percentage of error, based on the maximum vertical displacement, is very small. Note that the defocus from displacement and slope control is nearly identical to that from only displacement control. No advantage is demonstrated here by adding slope control.

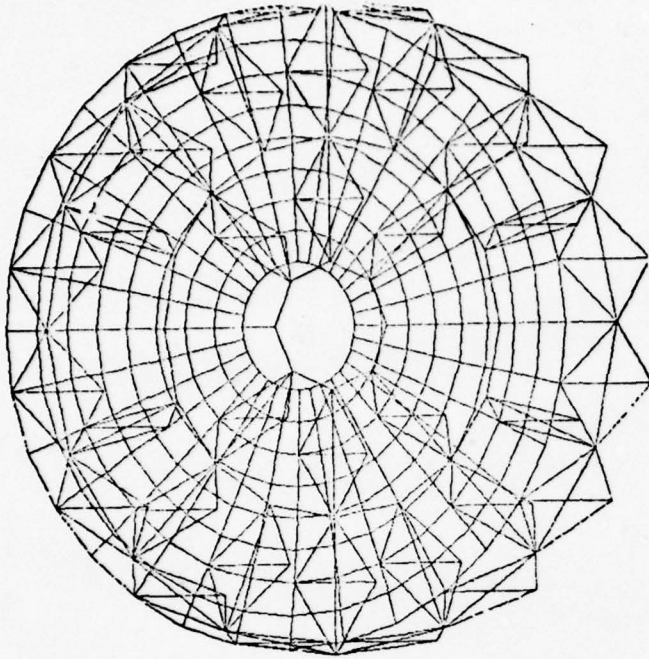
#### 40-Actuator System Finite Element Model

The finite element model of an active mirror system with 40 actuators and a 4-meter diameter primary mirror was generated using the Graphics-Oriented Interactive Finite Element Time-Sharing System (GIFTS) on an Eclipse minicomputer at the University of Arizona. GIFTS is an effective preprocessor for NASTRAN. The entire model was generated, plotted, and checked for accuracy using GIFTS in about a tenth the time of conventional methods. An interface program was written to convert the output data from GIFTS into input data for NASTRAN. Structural analyses were then performed on the model using the MSC/NASTRAN computer program on the AFWL Cyber 176 computer at Kirtland AFB, New Mexico. The same Eclipse minicomputer used to generate the model was configured to emulate a Control Data 200 User's Terminal that was connected by telephone to the AFWL computer.

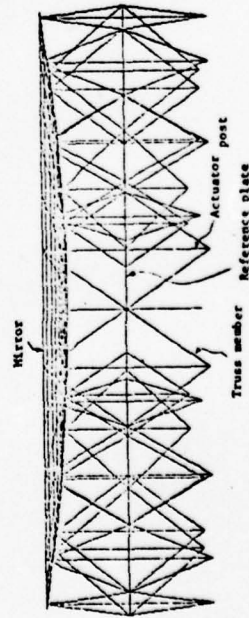
Three views of the mathematical model are shown in Fig. 21. In Fig. 21a, the top view, the actuators are designated by dark circles, and the six degrees of freedom supported at the reference plate are indicated. These six degrees of freedom on the periphery of the reference plate were constrained to zero motion for all analyses. Displacements  $u_x$ ,  $u_y$ , and  $u_z$  are displacements in the x, y, and z directions, while  $u_\phi$  is the displacement in



(a) Top view.



(c) Orthographic projection of top view rotated  $-30^\circ$  about x axis



(b) Side view.

Fig. 21. 40-actuator system. Undeformed shape.

a skewed direction, chosen so that the supports are kinematic. With this support the structure can distort due to the thermal loading without any restraint from the supports.

Individual structural members are identified in the side view, Fig. 21b. The model is composed of the following:

Mirror	256 plate elements
Reference plate	104 beam elements
Actuator Posts	80 beam elements
Truss Members	160 rod elements
Entire model	450 grid points

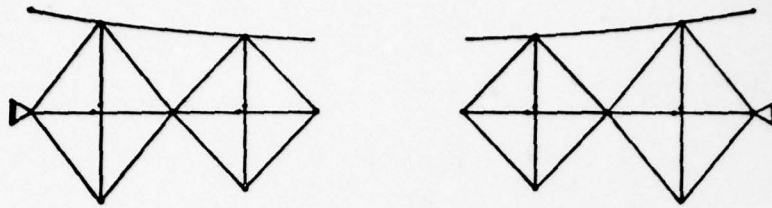
A sectional view of the model cut by the plane with  $y = 0$  is shown in Fig. 22a. At the intersections of the actuator posts and the reference plate, there are separate nodes for each structure, since the actuator posts pass through the reference plate. The individual nodes are shown slightly offset in the figure.

One of the individual trusses in Fig. 22a is shown in Fig. 22b, along with forces to cause in-plane slope control. The undeformed truss is shown in dashed lines and is superimposed with the deformed truss. The angular deflection of the mirror is due to both bending of the actuator post and to the movement of the ends of the actuator post. Out-of-plane slope control is produced by orienting the forces  $F$  normal to the plane of the truss.

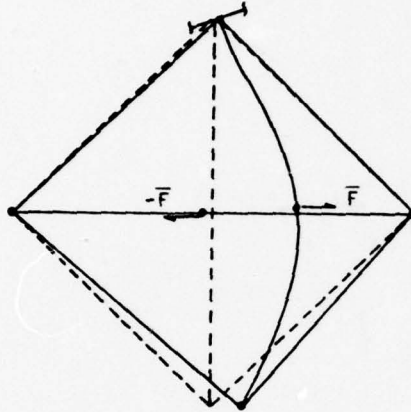
Forces needed for normal position control are shown in Fig. 22c.

#### MSC/NASTRAN Analysis to Design Mirror Support Structure

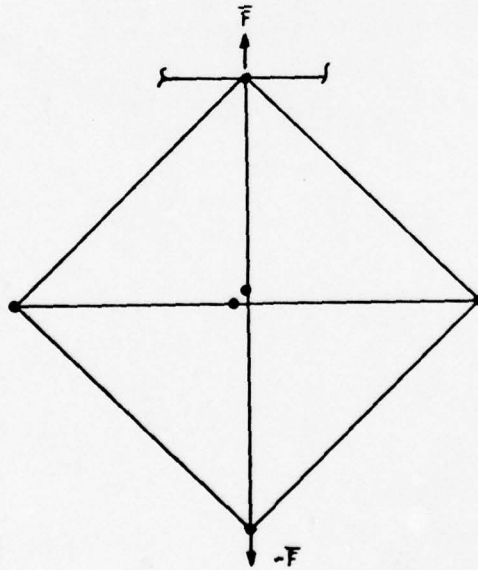
The structure supporting the mirror includes a reference plate, actuator posts, and truss members. The stiffness required of the mirror's support structure depends upon the mirror stiffness. Seven different mirrors



(a) Section View of the Finite Element Model Along the X-axis.



(b) Truss Deflections for In-plane Slope Control.



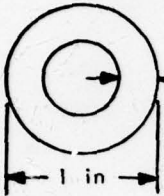
(c) Normal Position Control Truss Model

Fig. 22. Truss model and deflections.

and support structures were analyzed for a 40-actuator system. Figures 23 and 24 include sketches of cross sections of structural members, a mass summary, and material properties used for property sets 1, 6 and 7. The cross sections are drawn to scale. The mass summary does not include the mass of the actuators or any electronic equipment. Figures 25 through 33 show results of NASTRAN structural analyses of the three systems. These figures are contour plots of the surface of the mirror. Contour plots are included for each of the nine unique controls, i.e. for (1) normal position control, (ii) tangential slope control and (iii) radial slope control for an actuator located (a) 80 cm, (b) 160 cm, and (c) 200 cm from the center of the mirror. The loads in these analyses were unit loads, i.e., the magnitude of the loads in Figs. 25 through 33 is one dyne. Such a small load created very small displacements, but since the analysis is linear, results can be scaled. To evaluate the effectiveness of the support structure, these contour plots should be compared to those in Figs. 15 through 17 generated for a mirror with an infinitely rigid support structure.

Contour plots for property set 1 show that the deflection of one actuator is not localized to the mirror surface close to that actuator. Significant deflections occur across the entire mirror. This is totally unsatisfactory. It occurs since the bending stiffness of the mirror is too large compared to the stiffness of the support structure. To design a stiffer support structure, stiffnesses were calculated for each of the major components of the support structure, i.e. the reference plate, the truss members and the actuator posts, and then additional material was added where appropriate. For sets 6 and 7 the truss members were changed from steel wires, which would require pretensioning, to graphite epoxy truss rods, which could support compressive forces and therefore would not require pretensioning. This greatly simplifies initial assembly

Material Properties

	<u>Material</u>	<u>E (dyne/cm<sup>2</sup>)</u>	<u>ν</u>	<u>ρ (gm/cm<sup>3</sup>)</u>	<u>α (/°C)</u>
Steel Truss Wires ← .03 in →	Fused Silica	$7.31 \times 10^{11}$	.17	2.27	$.5 \times 10^{-6}$
Graphite Epoxy Actuator Posts 	Graphite Epoxy	$4.14 \times 10^{12}$	.3	2.77	—
	Steel	$2.07 \times 10^{12}$	.3	8.31	—

Note: (1) The properties for graphite shown above and used in the NASTRAN analysis are grossly in error. Those properties will be changed before studies are continued. We do not anticipate that this error will have a significant effect on results presented in this report, since compensating errors were made. Both the modulus of elasticity and density were too high. Consequently, the specific stiffness used, i.e.

$$E/\rho = 4.14 \times 10^{12} / 2.77 = 1.49 \times 10^{12} \text{ dyne-cm/gm}$$

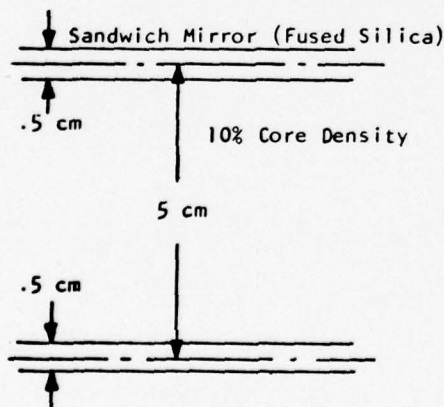
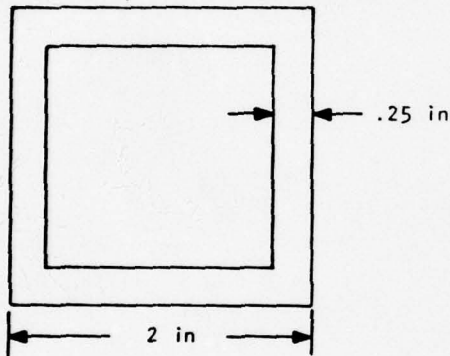
is only 7.2% above that for a proposed anisotropic

$$\text{GY-70 layup, i.e. } E/\rho = 2.15 \times 10^{12} / 1.55$$

$$= 1.39 \times 10^{12} \text{ dyne-cm/gm.}$$

(2) We are considering the use of composites with graphite fibers in a metallic matrix, instead of graphite epoxy. These include the graphite magnesium and graphite aluminum composites under development in DARPA contract F33615-78-5235.

Graphite Epoxy Reference Plate Bars



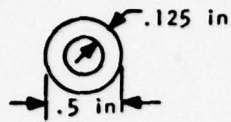
MASS SUMMARY

Mirror	397
Reference Plate	131
Actuator Posts	43
Truss Wires	.4
<u>Total Mass</u>	<u>571 kg</u>
Total Mass/ Mirror Surface Area	47 kg/m <sup>2</sup>

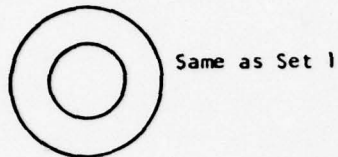
Fig. 23. Property set 1.

Property Set 6

Graphite Epoxy Truss Rods

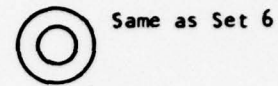


Graphite Epoxy Actuator Posts

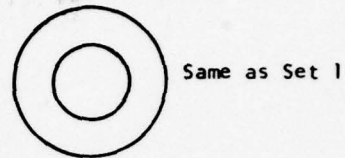


Property Set 7

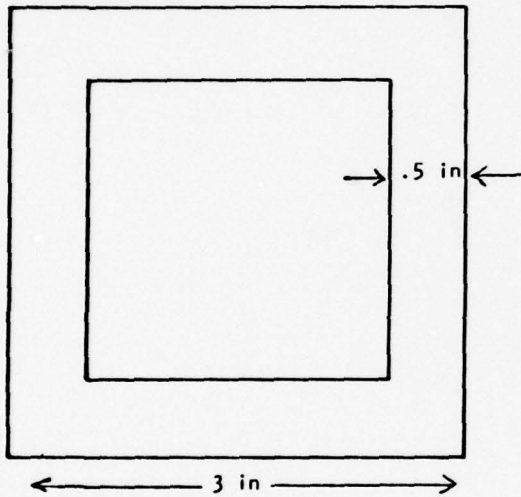
Graphite Epoxy Truss Rods



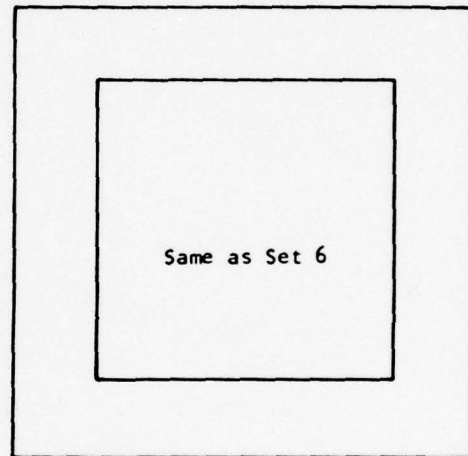
Graphite Epoxy Actuator Posts



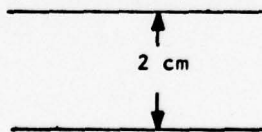
Graphite Epoxy Reference Plate Bars



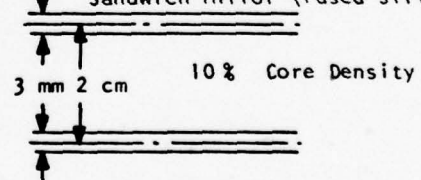
Graphite Epoxy Reference Plate Bars



Solid Mirror (Fused Silica)



Sandwich Mirror (Fused Silica)

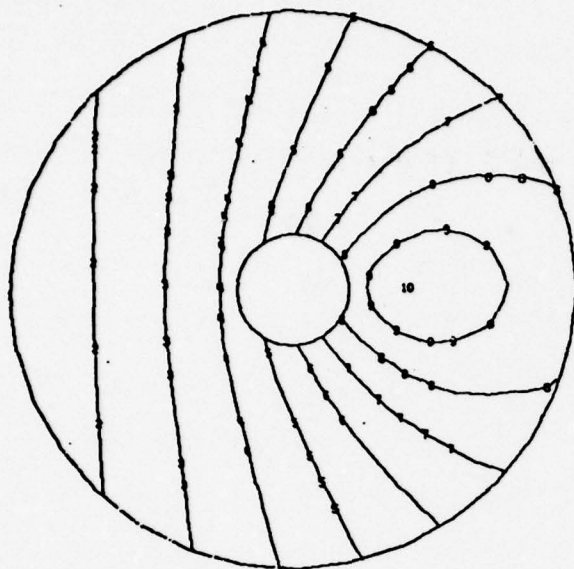


<u>MASS SUMMARIES</u>		
548	Mirror	211
375	Reference Plate	375
43	Actuator Posts	43
27	Truss Rods	27
<u>993</u> Kg	<u>Total Mass</u>	<u>656</u> Kg
82 Kg/m <sup>2</sup>	Total Mass/Mirror Surface Area	54 Kg/m <sup>2</sup>

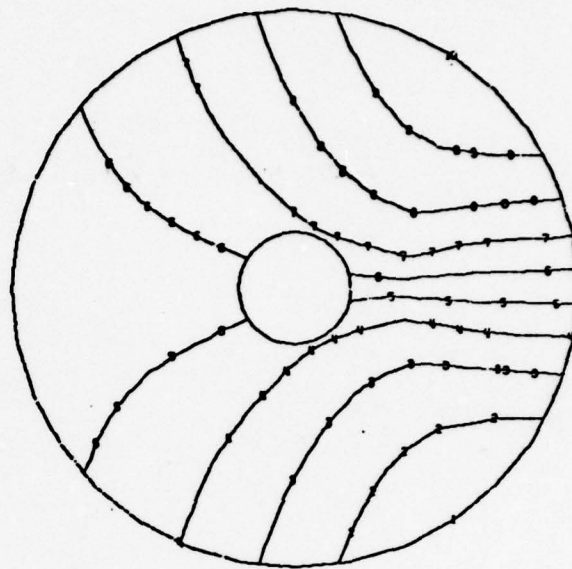
Fig. 24. Property sets 6 and 7.

MAX-DEF. =  $1.41 \times 10^{-13}$   
MIN-DEF. =  $-3.32 \times 10^{-14}$

MAX-DEF. =  $1.45 \times 10^{-10}$   
MIN-DEF. =  $-1.45 \times 10^{-10}$

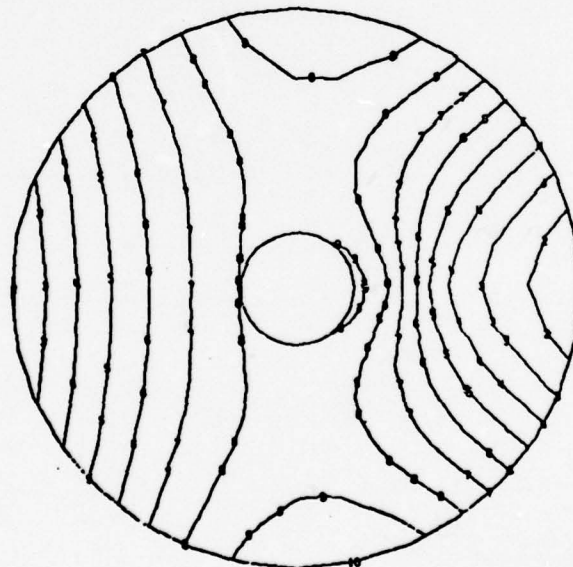


(a)



(b)

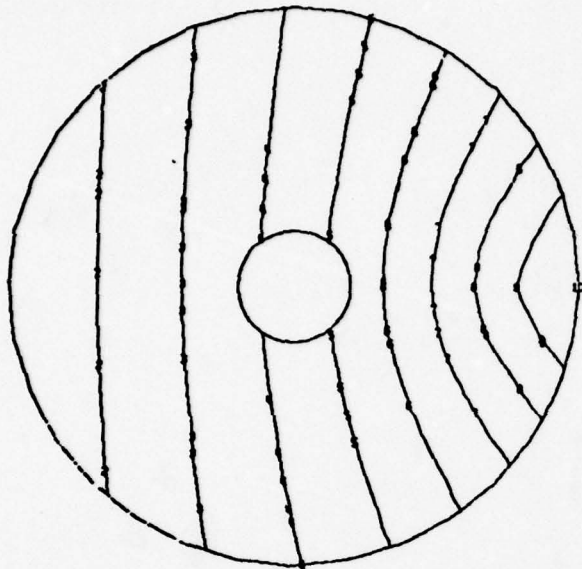
MAX DEF. =  $6.06 \times 10^{-11}$   
MIN DEF. =  $-1.85 \times 10^{-11}$



(c)

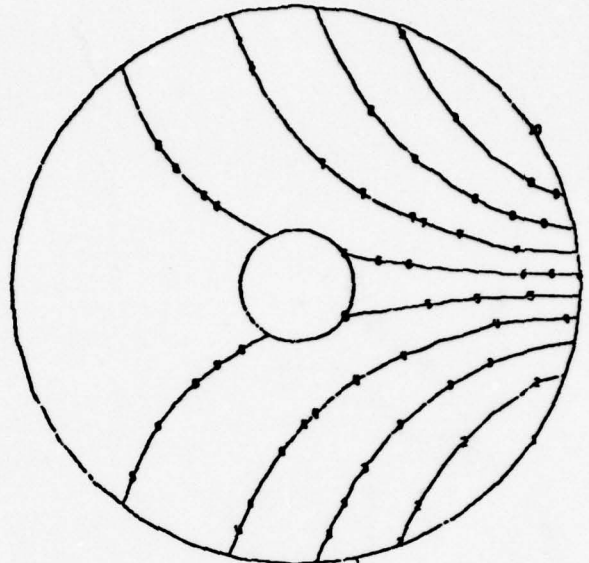
Fig. 25. 40-actuator system, 80-cm actuator. (a) Normal position control, (b) tangential slope control, and (c) radial slope control. Property set 1.

MAX-DEF. =  $5.61 \times 10^{-13}$   
MIN-DEF. =  $-7.13 \times 10^{-14}$



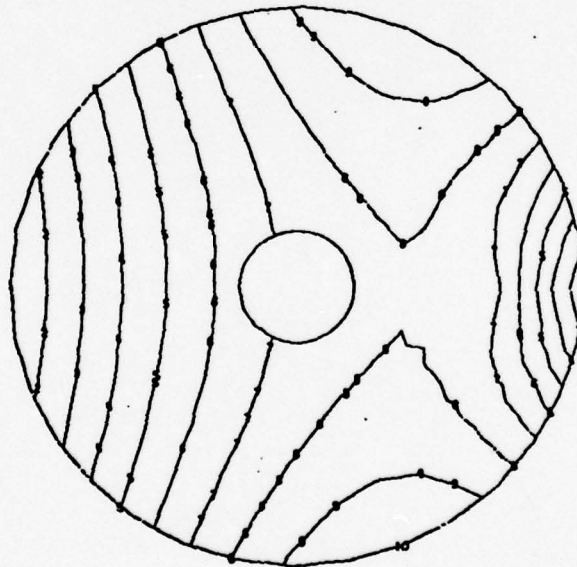
(a)

MAX DEF. =  $2.55 \times 10^{-10}$   
MIN DEF. =  $-2.55 \times 10^{-10}$



(b)

MAX-DEF. =  $1.30 \times 10^{-10}$   
MIN-DEF. =  $-3.60 \times 10^{-11}$

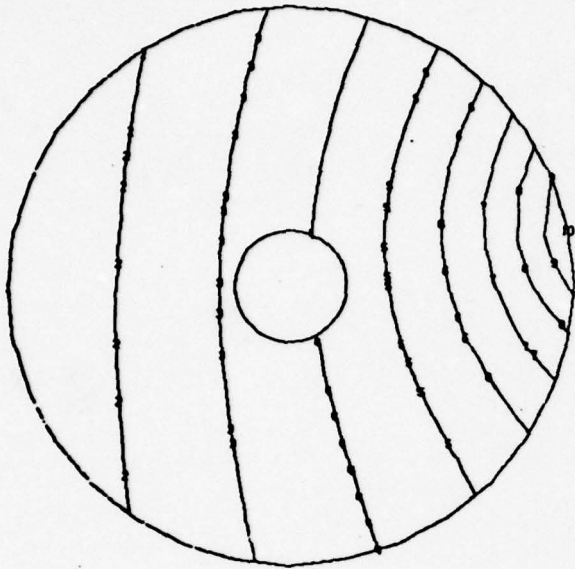


(c)

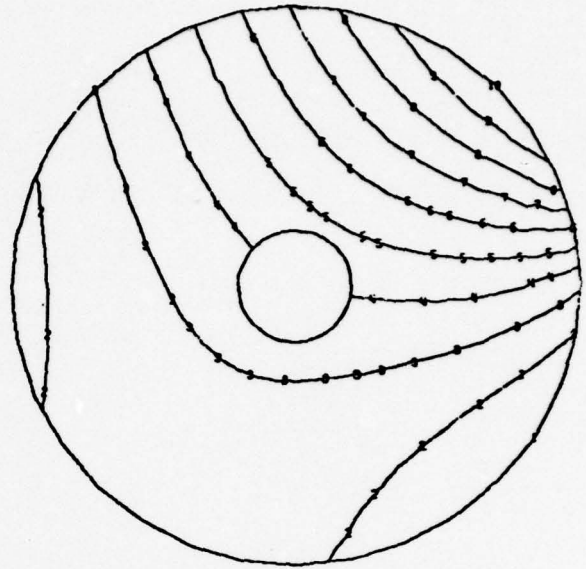
Fig. 26. 40-actuator system. 160-cm actuator. (a) Normal position control, (b) tangential slope control, and (c) radial slope control. Property set 1.

MAX DEF. =  $9.71 \times 10^{-13}$   
MIN DEF. =  $-8.14 \times 10^{-14}$

MAX DEF. =  $2.73 \times 10^{-10}$   
MIN DEF. =  $-5.62 \times 10^{-11}$

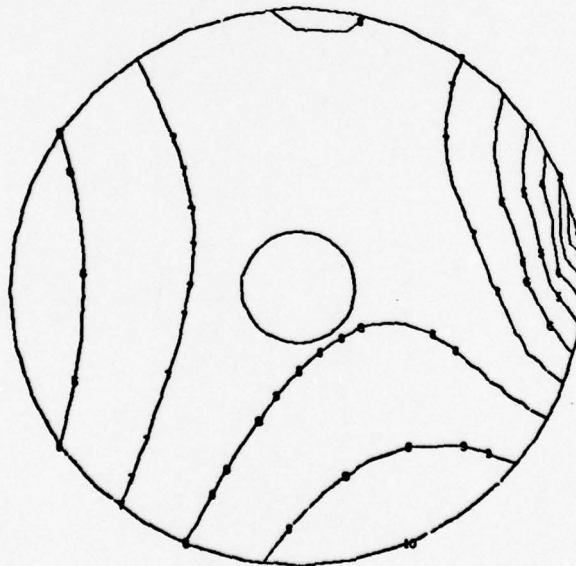


(a)



(b)

MAX DEF. =  $1.83 \times 10^{-10}$   
MIN DEF. =  $-2.33 \times 10^{-10}$

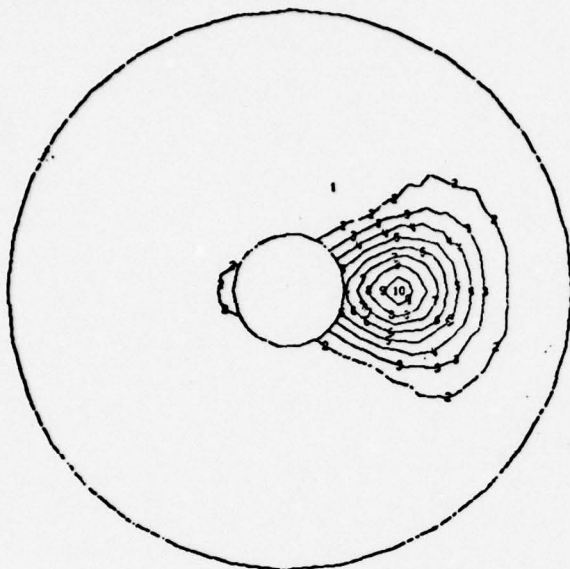


(c)

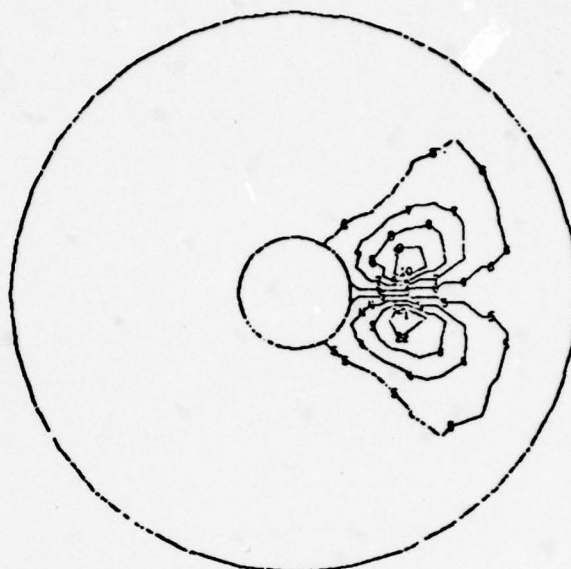
Fig. 27. 40-actuator system. 200-cm actuator.  
(a) Normal position control, (b) tangential slope control, and (c) radial slope control.  
Property set 1.

MAX DEF. =  $2.22 \times 10^{-12}$   
MIN DEF. =  $-1.67 \times 10^{-13}$

MAX DEF. =  $1.23 \times 10^{-10}$   
MIN DEF. =  $-1.23 \times 10^{-10}$

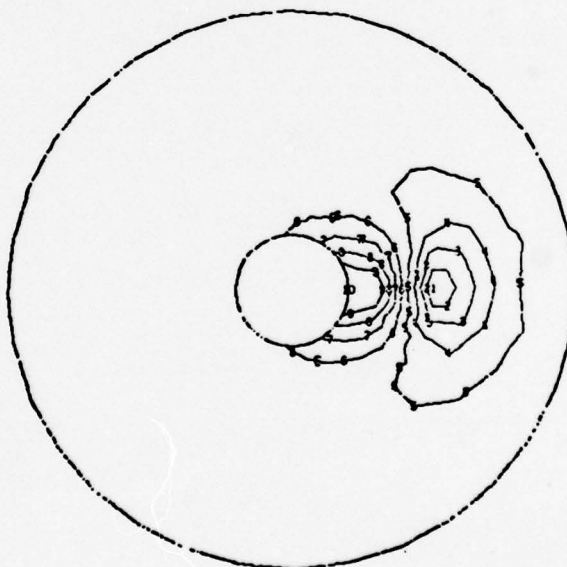


(a)



(b)

MAX DEF. =  $5.38 \times 10^{-11}$   
MIN DEF. =  $-4.71 \times 10^{-11}$

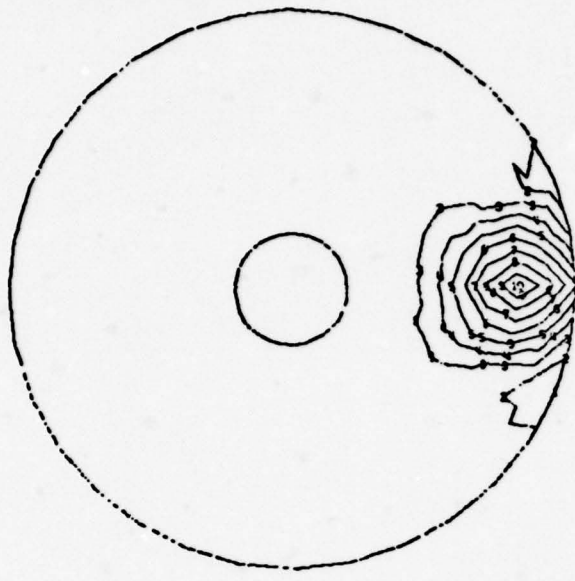


(c)

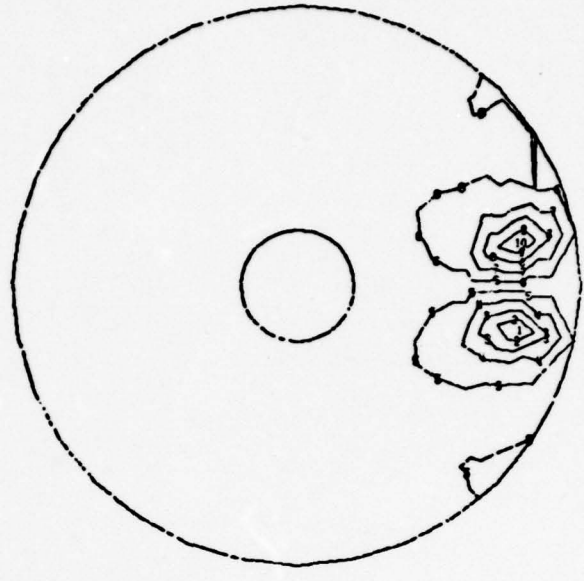
Fig. 28. 40-actuator system. 80-cm actuators.  
(a) Normal position control, (b) tangential slope control, and (c) radial slope control.  
Property set 6.

MAX DEF. =  $2.64 \times 10^{-12}$   
MIN DEF. =  $-5.06 \times 10^{-13}$

MAX DEF. =  $1.29 \times 10^{-10}$   
MIN DEF. =  $-1.29 \times 10^{-10}$

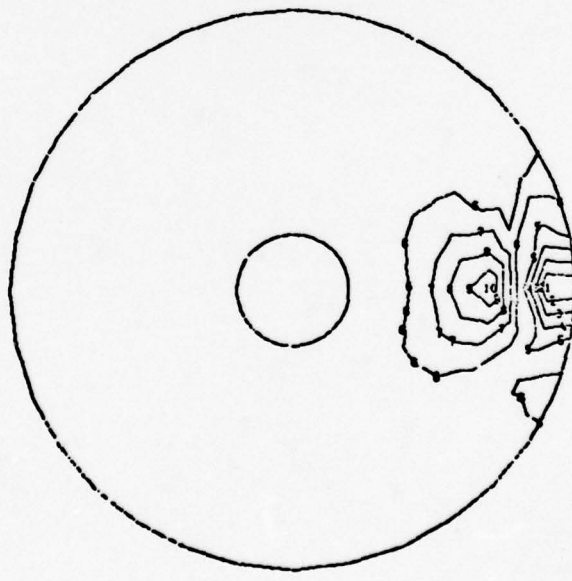


(a)



(b)

MAX DEF. =  $5.84 \times 10^{-11}$   
MIN DEF. =  $-5.07 \times 10^{-11}$

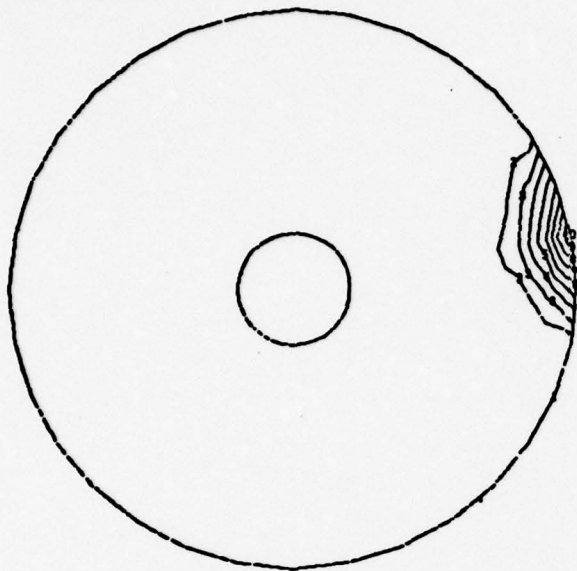


(c)

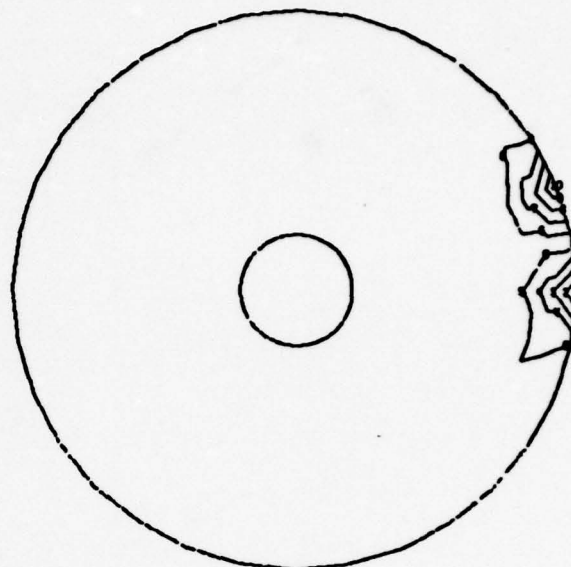
Fig. 29. 40-actuator system. 160-cm actuators.  
(a) Normal position control, (b) tangential slope control, and (c) radial slope control.  
Property set 6.

MAX DEF. =  $3.12 \times 10^{-12}$   
MIN DEF. =  $-1.95 \times 10^{-13}$

MAX DEF. =  $1.19 \times 10^{-10}$   
MIN DEF. =  $-1.00 \times 10^{-10}$

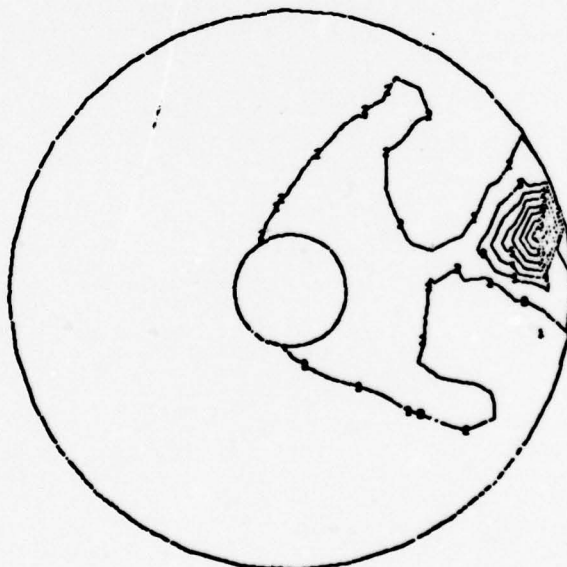


(a)



(b)

MAX DEF. =  $2.74 \times 10^{-10}$   
MIN DEF. =  $-2.89 \times 10^{-11}$

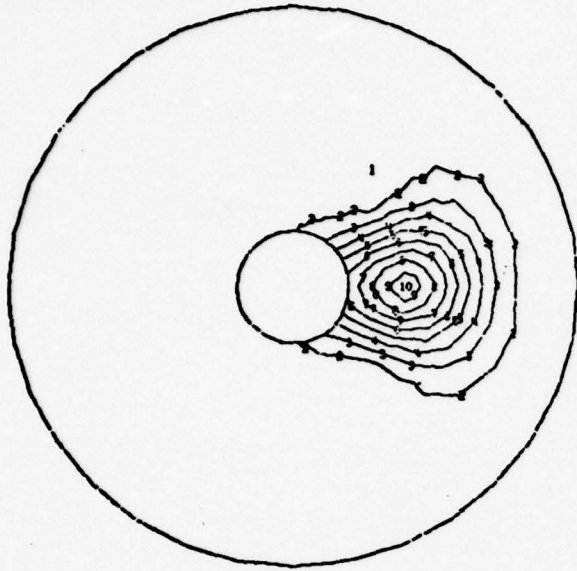


(c)

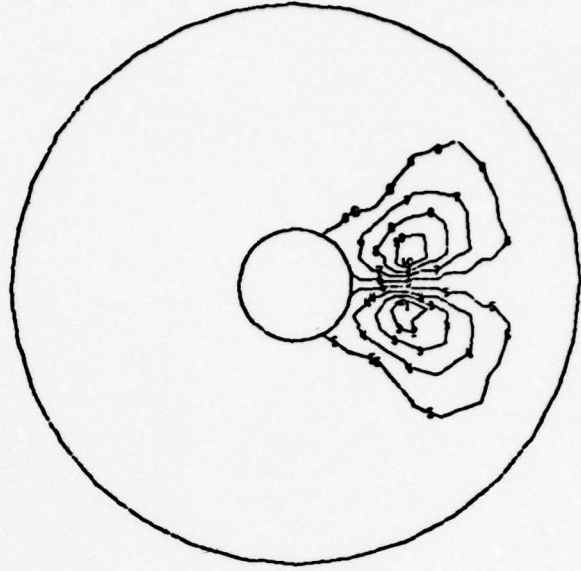
Fig. 30. 40-actuator system. 200-cm actuators.  
(a) Normal position control, (b) tangential slope control, and (c) radial slope control.  
Property set 6.

MAX DEF. =  $2.25 \times 10^{-12}$   
MIN DEF. =  $-1.39 \times 10^{-13}$

MAX DEF. =  $1.50 \times 10^{-10}$   
MIN DEF. =  $-1.50 \times 10^{-10}$

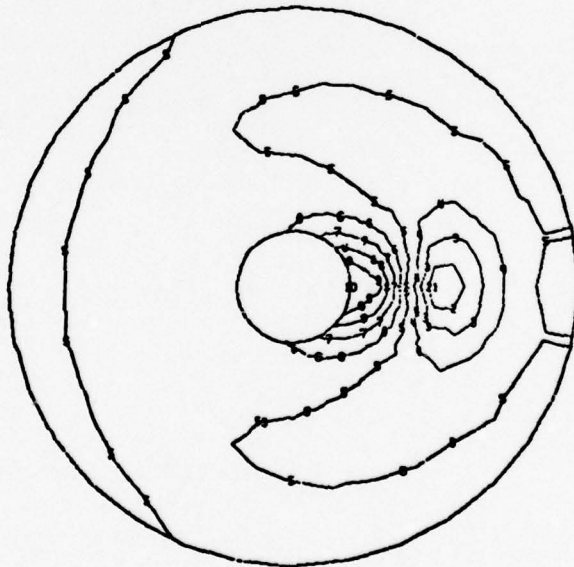


(a)



(b)

MAX DEF. =  $7.48 \times 10^{-11}$   
MIN DEF. =  $-5.87 \times 10^{-11}$

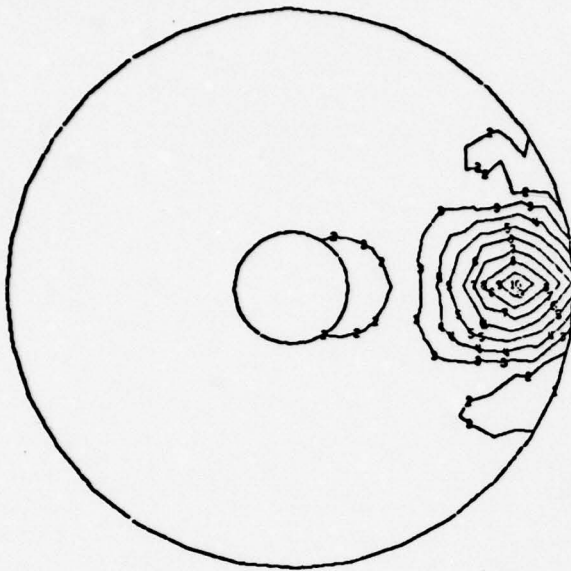


(c)

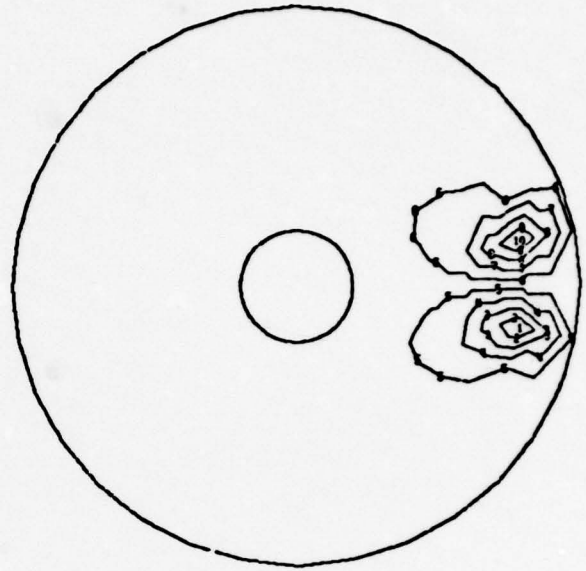
Fig. 31. 40-actuator system. 80-cm actuators.  
(a) Normal position control, (b) tangential slope control, and (c) radial slope control.  
Property set 7.

MAX DEF. =  $2.50 \times 10^{-12}$   
MIN DEF. =  $-4.50 \times 10^{-13}$

MAX DEF. =  $1.50 \times 10^{-10}$   
MIN DEF. =  $-1.50 \times 10^{-10}$

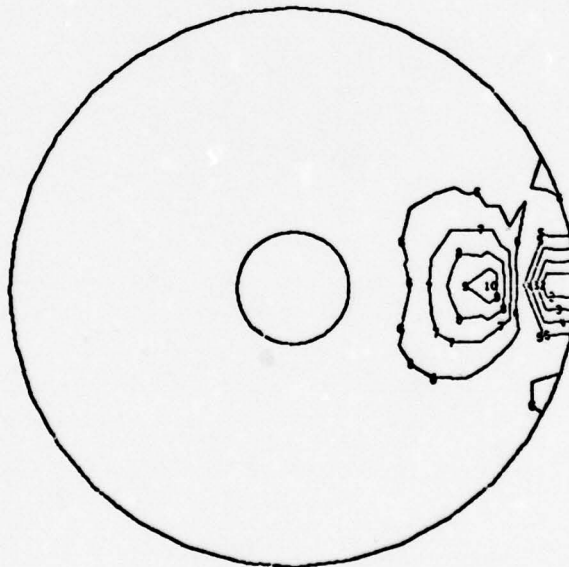


(a)



(b)

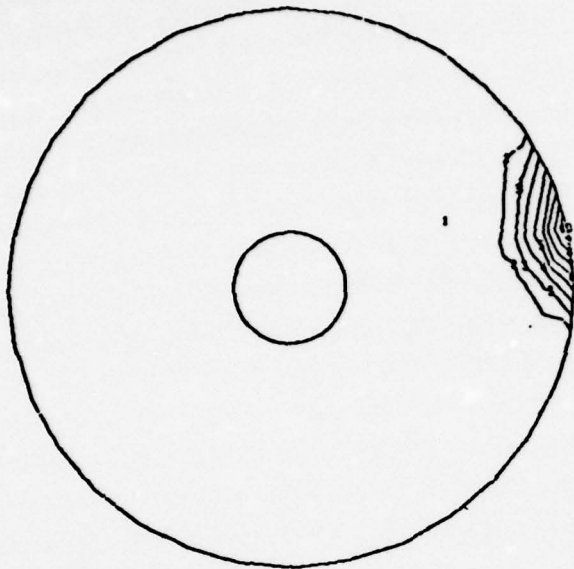
MAX DEF. =  $7.08 \times 10^{-11}$   
MIN DEF. =  $-6.89 \times 10^{-11}$



(c)

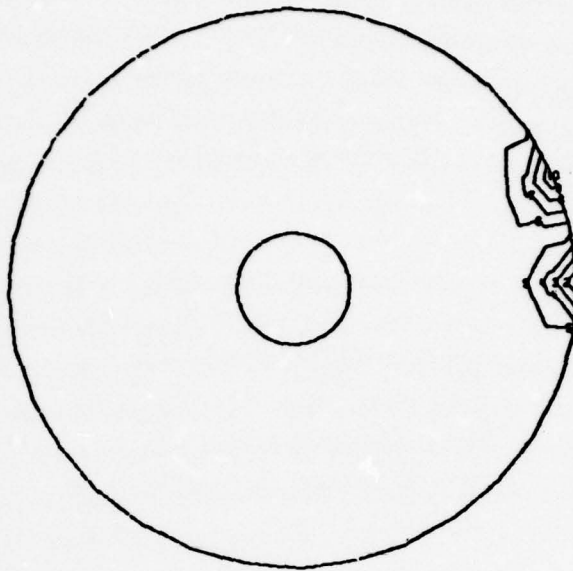
Fig. 32. 40-actuator system. 160-cm actuators.  
(a) Normal position control, (b) tangential slope control, and (c) radial slope control.  
Property set 7.

MAX DEF. =  $2.82 \times 10^{-12}$   
MIN DEF. =  $-4.65 \times 10^{-13}$



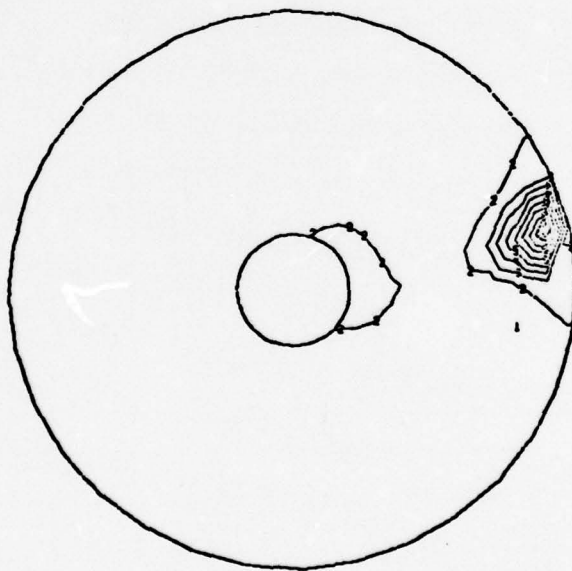
(a)

MAX DEF. =  $1.47 \times 10^{-10}$   
MIN DEF. =  $-1.34 \times 10^{-10}$



(b)

MAX DEF. =  $3.43 \times 10^{-10}$   
MIN DEF. =  $-3.44 \times 10^{-11}$



(c)

Fig. 33. 40-actuator system. 200-cm actuators.  
(a) Normal position control, (b) tangential slope control, and (c) radial slope control.  
Property set 7.

of the mirror system. In addition, the reference plate was thickened for these property sets.

A decision was made to analyze two systems employing fused silica mirrors. In one system the mirror is solid (property set 6) and in another it is of sandwich construction (property set 7). The cross section dimensions are higher than desired, but were chosen as being representative of the minimum feasible for a 4-m diameter mirror. Note that the solid mirror's mass of 548 kg is 1.2 times greater than the 445 kg mass of its support structure, while the sandwich mirror's mass of 211 kg is only 47% of its 445 kg support structure's mass. In neither system has the support structure been optimized to the minimal size required to support such mirrors. Since the bending stiffness of the solid mirror is 12% greater than for the sandwich mirror (a conservative estimate since the effect of shear deformation has been neglected), the mass of the sandwich mirror support structure could probably be reduced more than that for the solid mirror.

Contour plots of mirror deflection in Figs. 28 through 33 show that the support structures for property sets 6 and 7 perform well. Deflections are nearly as localized as for a system with a perfectly rigid support structure, depicted in Figs. 15 through 17. To provide a measure of the localization of deflection, consider the normal position control for each of the three unique actuator locations. For both property sets 6 and 7 the maximum mirror displacement at any non-controlled actuator is less than 2.6% of the mirror displacement of the controlled actuator. This illustrates the efficiency of this type of support structure.

## CHAPTER 5

### ANALYSIS TO EVALUATE DESIGN OF 40-ACTUATOR SYSTEM

#### Heat Transfer Analysis

Heat transfer analyses were performed to estimate temperatures across the mirror cross section. It was assumed that the axisymmetric axis of symmetry of the mirror was pointing toward the sun, so that the support structure was hidden in the shadow of the mirror. This would be a "worst case" of radiation input.

A one-dimensional steady state heat conduction analysis was performed, since it was assumed that thermal gradients from this type of analysis would be an upper bound. Using a heat transfer rate per unit area of  $q/A = 1 \text{ kW/m}^2$  for sunlight and assuming a 5% mirror coating absorptivity, the rate through the mirror becomes  $q/A = 50 \text{ W/m}^2$ . Temperatures from that analysis are shown in Fig. 34.

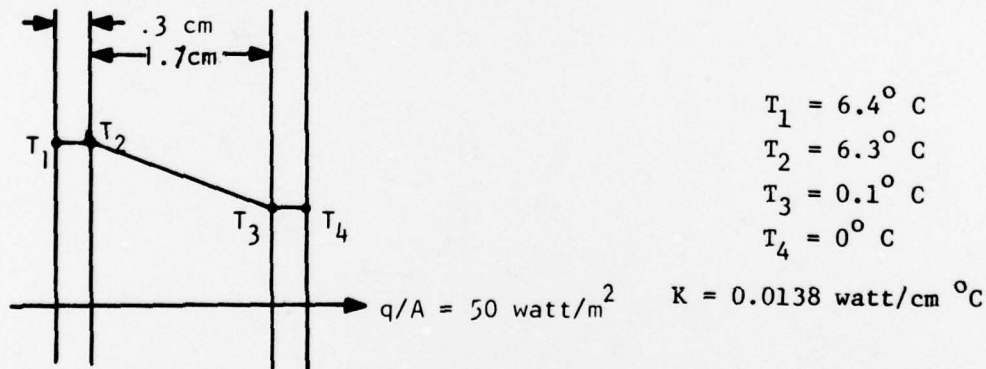


Fig. 34. Approximate thermal model.

Note that the temperatures are nearly constant through the front and rear face sheets. These temperatures were input to a NASTRAN structural analysis discussed in the next section. Since the analysis is linear, a change in the value of the temperature gradient can be accommodated by scaling of the results of the analysis.

Other heat transfer analyses that could be performed include (1) transient analyses to confirm that the temperature gradient due to steady-state heat conduction is indeed an upper bound, (2) two- and three-dimensional analyses, (3) heating of the support structure due to conduction and radiation, and (4) heating of the entire system due to orienting the system in different positions with respect to the sun. It may be desirable to utilize NASTRAN's heat transfer analysis capability in further refinements.

#### MSC/NASTRAN Analysis of 40-Actuator System

The remaining analyses to be described are (1) deflection of the mirror due to a thermal gradient through the mirror cross section and (2) defocus of the mirror. For these analyses the structural properties in set 7 were used. These analyses were preliminary in that they have uncovered problems and must be reaccomplished, but they are worth studying. The results indicate that the actuator placement in the central region of the mirror should be reconfigured.

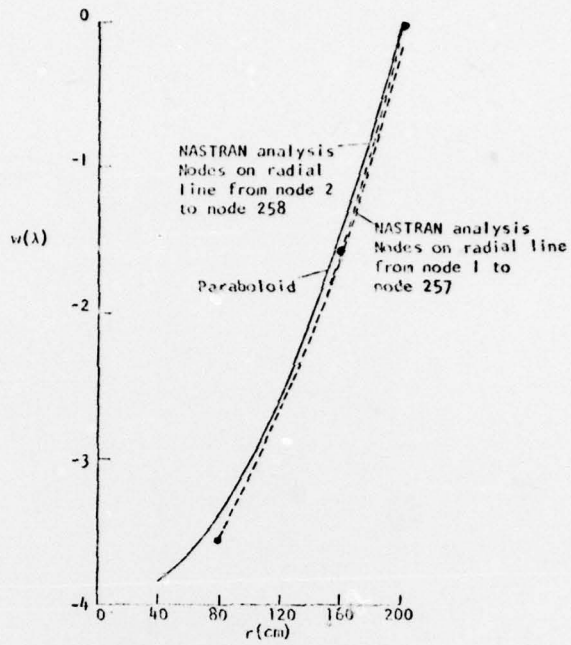
For both of these analyses, the first step was to determine deflections to be applied to actuator degrees of freedom. We used the same defocus described in Chapter 4, MSC/NASTRAN Analysis of a 40-Actuator Mirror, i.e. the deflection surface is an elliptic paraboloid and the equation for the  $z$  deflection is  $w = 1 \times 10^{-8} (r^2 - 200^2)$ . Due to the axis of symmetry, there are only three different values to calculate for actuator  $z$  deflection and radial slope. Deflections to correct for a thermal gradient are again simplified due to the existence of an axis of symmetry for the deflection surface. Deflections were found by executing a NASTRAN static analysis with the thermal gradient as the only load.

The second step in the analyses was to determine the actuator forces. These forces were calculated without regard to the coupling between actuator degrees of freedom. This coupling is inherent to a system with a support

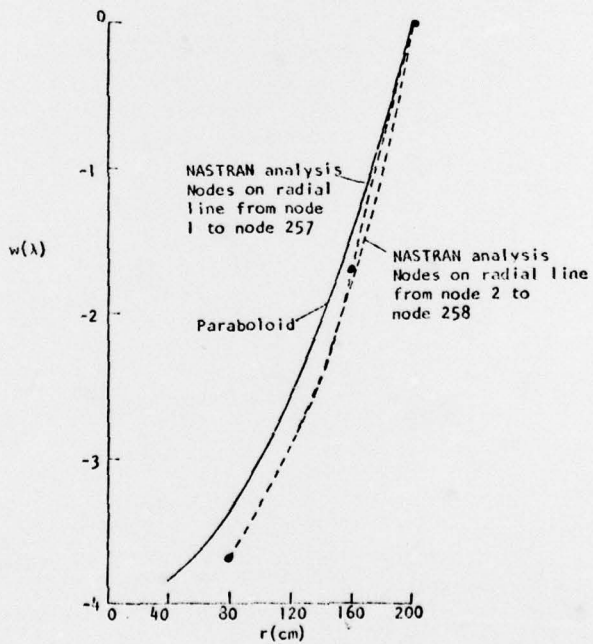
structure that has finite stiffness. The coupling results in errors in the  $z$  deflection and slope control of the actuators. These errors can be seen for defocus in Figs. 35a and 35b and for thermal gradient loading in Figs. 36a and 36b. These plots show  $z$  deflection of grid points on a radial line from the inner to the outer edge of the mirror. If the loading were exact (1) for defocus the solid circles, indicating actuators, would lie on the solid curve and (2) for the thermal gradient the solid circles would lie on the line of zero deflection. These errors indicate the need for a control system that can accommodate a small degree of coupling in degrees of freedom of the mechanical system.

The contour plots for defocus are Figs. 37a and 37b. Note that contour lines are flattened more than in the contour plots, Fig. 19, for the analysis of the mirror. This is primarily due to the coupling effect discussed in the previous paragraph. Figure 38 is a contour plot of the surface of the mirror due to thermal expansion caused by the thermal gradient. Figures 39a and 39b are contour plots of the correction introduced by (a) actuator normal position control and by (b) actuator normal position control combined with radial slope control, respectively. Figures 40a and 40b are contour plots of the mirror surface after these corrections have been made, i.e. they are the superposition of the previous two sets of contour plots.

The figures for the thermal gradient loading show that, due to the greater thermal expansion of the top face of the mirror as compared to the bottom face, both the inner and outer edges of the mirror curl toward the rear. Actuators along the outer edge of the mirror reduce the curling, but between actuators scalloping takes place. The scalloping probably cannot be stopped altogether. Since there are no actuators along the inner edge of the mirror, the curling could not be restrained on the inner edge. It will probably be necessary to add actuators along the inner edge, but even then some scalloping will exist

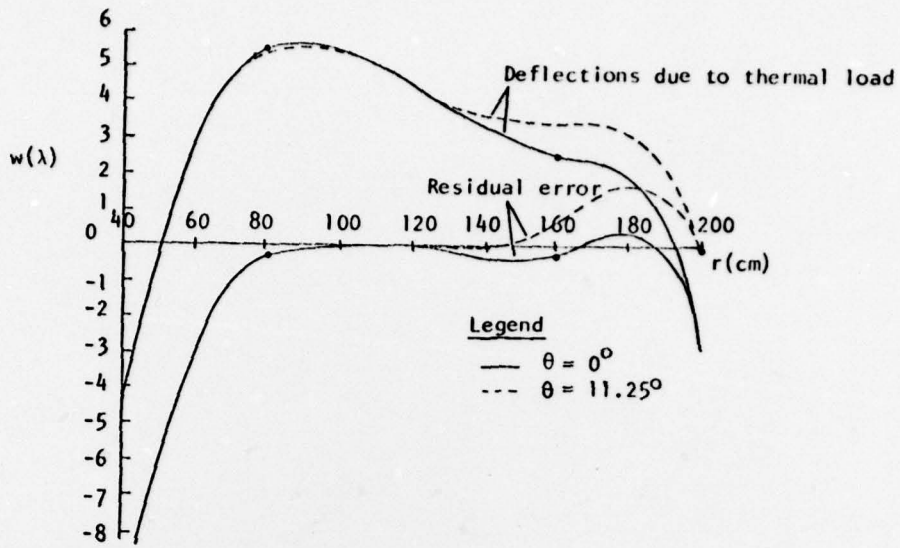


(a)

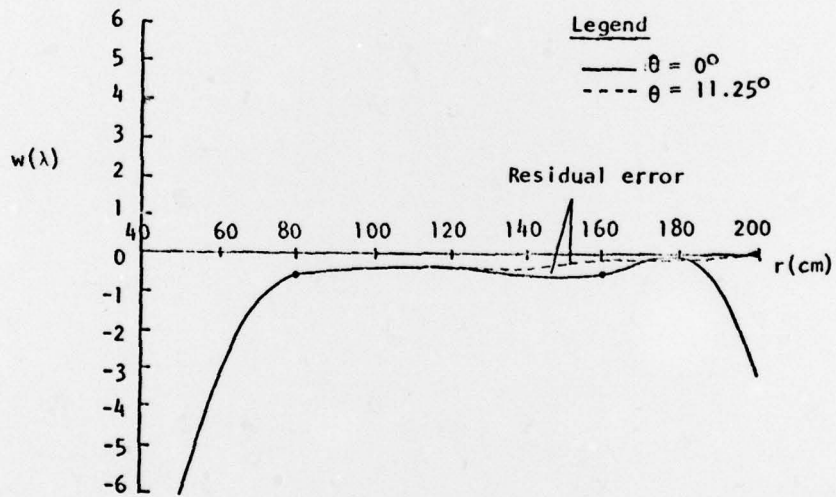


(b)

Fig. 35. Deflection of radial cross section of mirror during defocus with (a) only actuator normal position control, and (b) actuator normal position and radial slope controls.



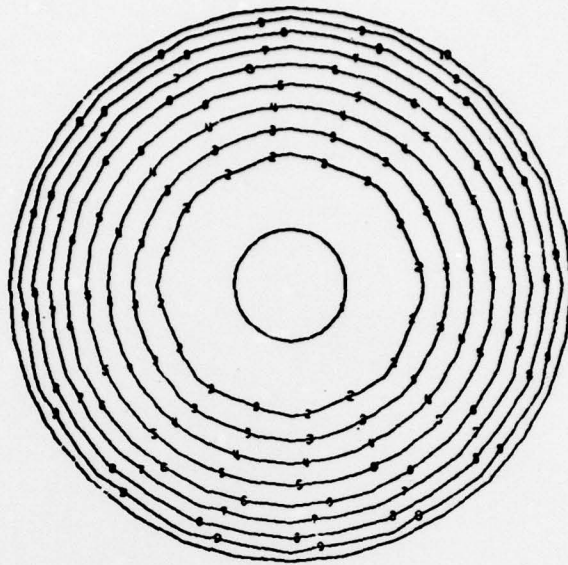
(a)



(b)

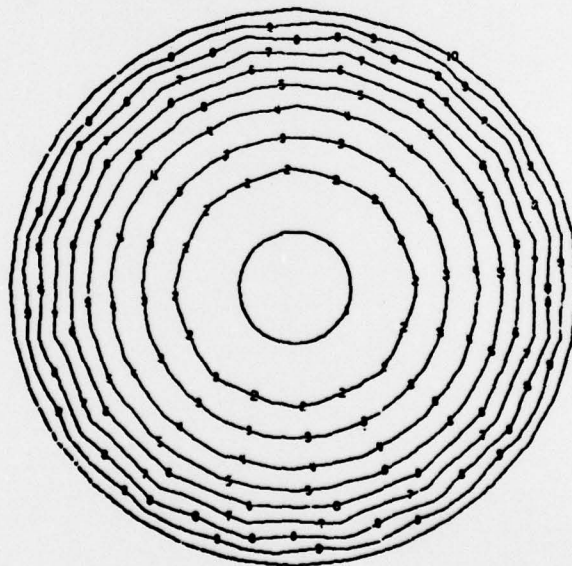
Fig. 36. Deflection of radial cross section of mirror heated by thermal gradient and with (a) actuator normal position control and (b) actuator normal position and radial slope control.

MAX-DEF. = -  $1.95 \times 10^{-6}$   
MIN-DEF. = -  $3.65 \times 10^{-4}$



(a)

MAX-DEF. = -  $3.57 \times 10^{-7}$   
MIN-DEF. = -  $4.01 \times 10^{-4}$



(b)

Fig. 37. Contour plots for defocus from (a) actuator normal position control and (b) actuator normal position and radial slope control. Property set 7.

MAX-DEF. =  $5.47 \times 10^{-4}$   
MIN-DEF. =  $-4.28 \times 10^{-4}$

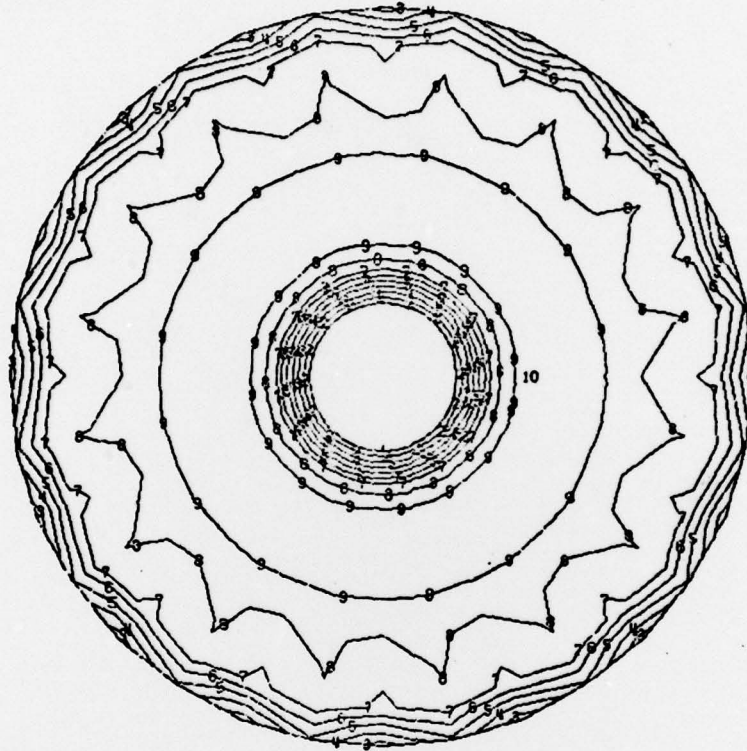
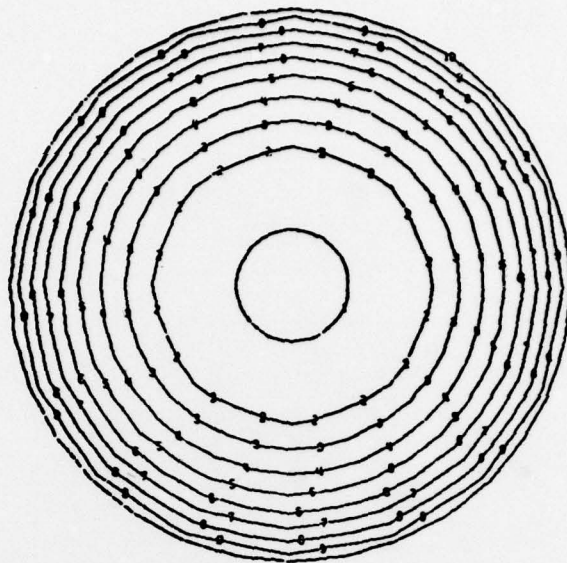


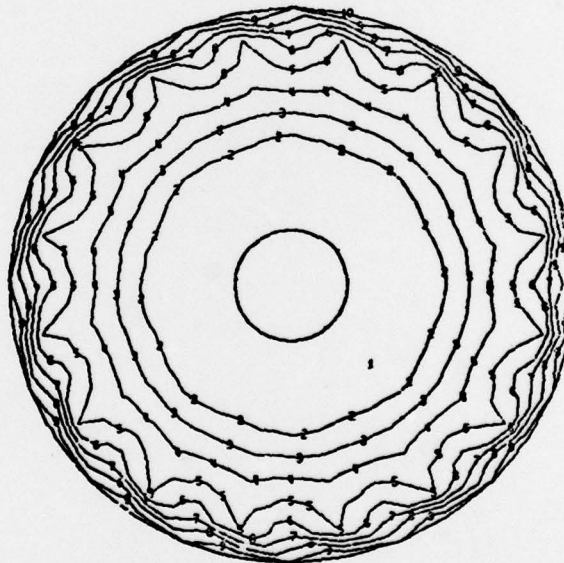
Fig. 38. Contour plot of deflection of mirror heated by thermal gradient and with no actuator control. Property set 7.

MAX-DEF. =  $1.04 \times 10^{-5}$   
MIN-DEF. =  $-5.83 \times 10^{-4}$



(a)

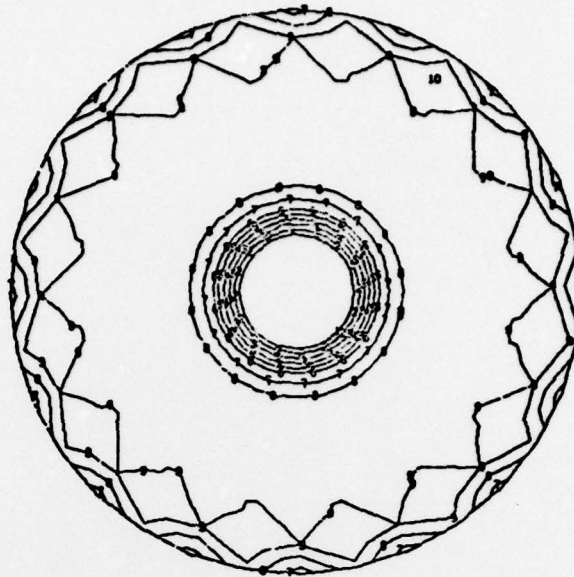
MAX-DEF. =  $1.84 \times 10^{-5}$   
MIN-DEF. =  $-6.02 \times 10^{-4}$



(b)

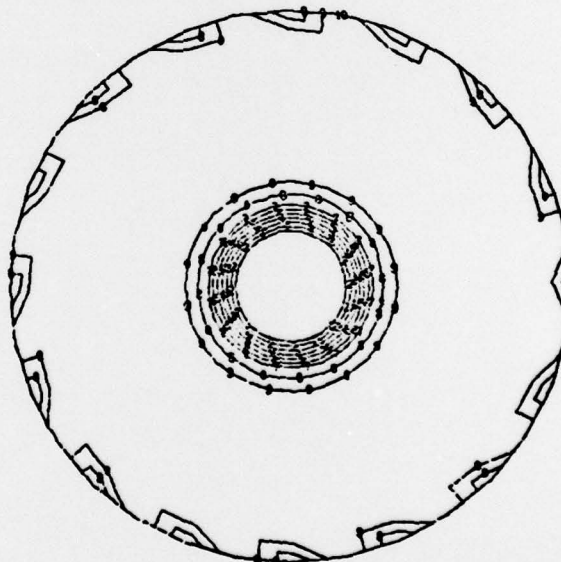
Fig. 39. Contour plots of deflection from (a) actuator normal position control and (b) actuator normal position and radial slope control. Property set 7.

MAX-DEF. =  $1.67 \times 10^{-4}$   
MIN-DEF. =  $-1.01 \times 10^{-4}$



(a)

MAX-DEF. =  $4.67 \times 10^{-6}$   
MIN-DEF. =  $-9.66 \times 10^{-4}$



(b)

Fig. 40. Contour plots of heated mirror after (a) normal position control and (b) actuator normal position and radial slope control. Property set 7.

between these new actuators, just as it does between actuators on the outer edge.

The efficiency of the support structure simplifies the task of the active control system. To measure the efficiency of the support structure we calculated the RMS value of the deflection of the mirror due to a thermal gradient load. The result for the fused silica mirror was  $w_{RMS} = 2.44 \lambda$ . If the mirror were made of ULE or CerVit, linear analysis allows us to arrive at the new RMS deflection by the following simple formula:

$$w_{RMS}^{(ULE)} = \frac{w_{RMS}^{(Fused\ Silica)} \alpha^{(ULE)}}{\alpha^{(Fused\ Silica)}} \\ = \frac{2.44\lambda \times .03 \times 10^{-6}}{0.5 \times 10^{-6}} = 0.146\lambda.$$

This can be considerably reduced by placing actuators along the inner edge of the mirror. This low RMS value is extremely significant. By using actuators which lock in position when turned off, the active figure control system may not have to be turned on when the mirror is exposed to sunlight. This would greatly simplify the role of the active control system, by relying on the "passive" inherent stiffness of the structure of the integrated active mirror.

It should again be reiterated that the results reported in this section are preliminary. Specifically, to illustrate one problem with the present analyses, refer to Fig. 22. That figure shows that at the locations where the actuator posts pass through the reference plate, there are separate nodes for the posts and the plate. When using high stiffness position actuators rather than low stiffness force actuators, actuator posts are essentially rigidly attached to the reference plate for the degrees of freedom without

enforced displacements. In the analyses the actuators were low stiffness force actuators rather than high stiffness position actuators. This explains why in Fig. 36 the outer edge of the mirror curls severely due to the thermal gradient. The entire structure will be much stiffer when the actuator stiffnesses are increased.

## CHAPTER 6

### CONCLUSIONS

Experimental results, though incomplete, support the 40-actuator integrated active mirror system finite element model in a qualitative way. Some discrepancy in the detailed matching between theory and experiment was to be expected, because the computer model was set up for the entire system including a lightweight reference plate. The stiffer experimental structure should result in more localized effects.

There are no significant differences in results whenever SAP IV and MSC/NASTRAN finite element models of identical structures were analyzed.

NASTRAN analyses were performed to design a mirror support structure stiff enough that deflection of the mirror surface due to control of one actuator degree of freedom was localized to the immediate vicinity of the actuator. Structures were not optimized to minimize weight. These analyses resulted in the following results:

	<u>Solid Mirror</u>	<u>Sandwich Mirror</u>
<u>Physical Dimensions</u>	2 cm thick	3 mm thick faces 10% density, 1.7 cm thick core
<u>Mirror Mass (kg)</u>	548	211
<u>Support Structure Mass (kg)</u>	445	445
<u>Total System Mass (kg)</u>	993	656

First-cut heat transfer analysis shows that sunlight causes a  $6.4^{\circ}$  C thermal gradient between the front and rear surfaces of the mirror.

Further analysis is much more complicated and would have to be performed with the aid of NASTRAN.

NASTRAN analyses due to defocus and to a thermal gradient through the mirror are preliminary, but they indicate a significant design change to the 40-actuator system. Due to edge effects, eight tangential actuators must be positioned along the inner edge of the mirror hole. The thermal analysis indicates that part of the role of the active control system may be assumed by the inherent stiffness of the structure of the integrated active mirror. This simplifies the task of the active control system.

### Bibliography

- Bathe, K.J., E.L. Wilson, and F.E. Peterson, "A Structural Analysis Program for Static and Dynamic Response of Linear Systems," EERC-75-11, College of Engineering, Berkeley, California, 1973.
- Joseph, Jerrard A., "MSC/NASTRAN Application Manual," CDC Version, The MacNeal-Schwendler Corporation, Los Angeles, California, January 1979.
- Radau, R.E. Jr., "Analysis and Design of an Active Thin Shell Mirror," MS Thesis, University of Arizona, 1977.
- Shannon, R.R., W.S. Smith, Final Report on Active Mirror Holographic Interferometry, The University of Arizona, 78 pp., September 1978.
- Timoshenko, S., Woinowsky-Krieger, S., Theory of Plates and Shells, McGraw-Hill, Inc., Second Edition, 1959.